

# 1 **Water flow timing, quantity, and sources in a fractured high mountain**

## 2 **permafrost rock wall**

3 Matan Ben-Asher<sup>1</sup>, Antoine Chabas<sup>2</sup>, Jean-Yves Josnin<sup>2</sup>, Josué Bock<sup>2</sup>, Emmanuel Malet<sup>2</sup>, Amaël  
4 Poulain<sup>3</sup>, Yves Perrette<sup>2</sup>, Florence Magnin<sup>2</sup>

5 <sup>1</sup>Department of Natural Sciences, Open University of Israel, Ra'anana, Israel

6 <sup>2</sup>EDYTEM, USMB, CNRS, 5 bd de la mer Caspienne, 73376 Le Bourget du Lac cedex, France

7 <sup>3</sup>TRAQUA S.A., Namur, Belgium

8

9 *Correspondence to:* Matan Ben-Asher ([matanbe@openu.ac.il](mailto:matanbe@openu.ac.il)) and Florence Magnin ([Florence.Magnin@univ-smb.fr](mailto:Florence.Magnin@univ-smb.fr))

### 10 **Abstract**

11 Water flow in high mountain rock walls is crucial for landscape evolution and slope stability. However, the timing, quantity,  
12 and sources of this flow remain poorly understood. In the Mont Blanc massif, tunnels at the Aiguille du Midi peak (3842 m)  
13 provide direct access to steep permafrost-affected rock walls. Between May 2022 and October 2023, we monitored water  
14 flowing from fractures using a real-time system that measured flow rate, temperature, electrical conductivity, and fluorescence  
15 of tracers, alongside meteorological data and ground surface temperatures.

16 The results indicate high surface–subsurface connectivity. The water source is primarily snowmelt, with additional inputs from  
17 late-summer rainfall. Electrical conductivity, stable isotopes, and recession curve analysis suggest another source of older  
18 subsurface ice. Flow onset was closely tied to air temperatures, with steady diurnal fluctuations appearing once rock surface  
19 temperatures exceeded 0 °C. Lag times between daily peaks of flow rate and peaks of air and ground surface temperatures of  
20 3–9 hours and 0–3 hours, respectively, point to rapid unsaturated infiltration conditions. Distinct flow regimes observed in two  
21 adjacent fracture systems reflect a complex, heterogeneous network, including sediment-filled fractures with a delayed  
22 response. Significant flow rates (often >10 L/h) and water temperature often exceeding 5 °C, suggest significant heat transfer  
23 by advection, capable of enhancing permafrost degradation.

24 This study provides rare direct observations of fracture flow dynamics in steep permafrost rocks, and improves our  
25 understanding of water routing and its response to atmospheric forcing. The findings offer valuable constraints for coupled  
26 hydrothermal models, permafrost-related hazard assessments, and the potential impact of climate change.

27

28 **Key words:** Permafrost, monitoring, water infiltration, Mont Blanc massif, climate change

## 29 1. Introduction

### 30 1.1. Hydrogeology of high mountains

31 Water plays a crucial role in weathering and erosion processes in mountainous landscapes. In the periglacial belt, the presence  
32 of water in the shallow subsurface can cause rock fracturing through ice segregation or volumetric expansion, depending on  
33 temperature conditions and saturation levels (Draebing and Krautblatter, 2019; Matsuoka and Murton, 2008). Hydrostatic  
34 pressure in undrained fractures can drive catastrophic failure (Hasler et al., 2012; Krautblatter et al., 2013; Scandroglio et al.,  
35 2021; Walter et al., 2020). Over geological time scales water is a key catalyst of mechanical rock weathering processes related  
36 to subcritical cracking (Eppes and Keanini, 2017). The melting of ice in joints under thawing conditions can release detached  
37 blocks and lead to debris and rock falls, and the formation of scree slopes (Hales and Roering, 2007). Water infiltration in  
38 bedrock may also trigger large rock slope failures by reducing the friction of rough fracture contact surfaces (Krautblatter et  
39 al., 2013). In permafrost ground, the presence of sealing ice in pores and fractures favors the development of high hydrostatic  
40 pressures (Fischer et al., 2010; Marcer et al., 2020), which may increase the frequency or magnitude of mass movements. In  
41 addition to mechanical pressure, water circulation can also cause thermal perturbations with potential cooling effects in some  
42 cases (Maréchal et al., 1999; Phillips et al., 2016) or warming effects in others (Hasler et al., 2011; Phillips et al., 2016). In  
43 permafrost ground, heat advection from water infiltration could accelerate permafrost degradation (Gruber and Haeberli, 2007;  
44 Hasler et al., 2011; Magnin and Josnin, 2021), and potentially develop thawing corridors (Krautblatter and Hauck, 2007;  
45 Keushing et al., 2017). Recent observations of increased rock fall activity in high mountains regions have been linked to  
46 permafrost degradation (Allen et al., 2009; Fey et al., 2025; Gruber et al., 2004; Huggel et al., 2012; Legay et al., 2021; Ravanel  
47 et al., 2017; Ravanel and Deline, 2011). The warming of intact frozen rock is commonly related to rockwall destabilization  
48 due to a decrease in rock uniaxial and tensile strength (Dwivedi et al., 1998; Krautblatter et al., 2013; Li et al., 2003; Mellor,  
49 1973). Water-related processes have been suggested as a potential cause of several rock fall events (Cathala et al., 2024;  
50 Erismann and Abele, 2001; Scandroglio et al., 2021; Strauhal et al., 2016). However, while hydrogeological studies in alpine  
51 permafrost have primarily focused on coarse-grained terrain, such as rock glaciers (Bast et al., 2024) and scree slopes (Pellet  
52 and Hauck, 2017), little is known about water dynamics within bedrock rockwalls—despite their critical role in slope stability  
53 and landscape evolution.

### 54 1.2. Existing knowledge on water flow and infiltration in mountain permafrost

55 In steep alpine bedrock, the question of water infiltration and its thermal and mechanical implications is crucial but is rarely  
56 addressed directly (Krautblatter et al., 2013). Studying hydrogeological processes in these environments poses several  
57 challenges, including limited accessibility, the hidden nature of water flow pathways, strong spatial and temporal variability,  
58 non-linear system behavior, and the difficulty of identifying water sources quantitatively. Hasler et al. (2011) used numerical  
59 simulations to explore the impact of advective heat transport by water percolation on subsurface temperatures and ice-level

60 changes. In the absence of hydrogeological field measurements, they performed laboratory experiments and demonstrated  
61 significant implications for the role of water flow in thaw-related instabilities in cold mountain permafrost regions. Maréchal  
62 et al. (1999) used a hydrothermal model to simulate an observed thermal anomaly that was found during drilling work in the  
63 road tunnel under the Mont-Blanc massif and showed that infiltration of water from the surface contributed to the continuous  
64 cooling of the alpine massif at depth. Ben-Asher et al. (2023) estimated the potential water input in steep alpine bedrock using  
65 field measurements and numerical simulations.

66 Apart from indirect studies (Ben-Asher et al., 2023; Hasler et al., 2011; Maréchal et al., 1999; Scherler et al., 2010), few studies  
67 have attempted to directly monitor groundwater flow in steep, permafrost-affected alpine environments (Gabrielli et al., 2012;  
68 Manning and Caine, 2007). In a recent study, Scandroglio et al. (2025) measured water outflow in 55 m deep fractures under  
69 the permafrost-affected Zugspitze Ridge (2815–2962 m a.s.l). They compared their dataset with meteorological data and a  
70 snowmelt model to infer the timing and quantity of water flow and constrain the hydrological pressure in the fractures. They  
71 also analyzed recession curves of the measured flow rate, a technique that was never applied to alpine rock fractures before.

### 72 **1.3. Saturated and non-saturated flow**

73 From a hydrogeological perspective, a fractured summit is more accurately described as a permeable infiltration zone than as  
74 an aquifer. However, due to the scarcity of drilling data, constraints on the thickness of the high-elevation alpine unsaturated  
75 zone remain highly limited (Maréchal, 1998). The first tests of hydrodynamical models of a high alpine and permafrost-  
76 affected rock wall site were performed by Magnin & Josnin (2021) on the Aiguille du Midi site. This study showed that the  
77 unsaturated zone is probably more than 1000 m thick. In the Rocky Mountains, several hundred meters of unsaturated zone  
78 above the water table have also been reported (Russell et al. 2001).

79 Generally, unsaturated conditions apply in soils, permeable rocks, and deposits, and water flow is often considered subvertical  
80 and evaluated using the Richards equation (Smith, 2002). In crystalline rock settings, porosity and permeability are essentially  
81 controlled by the geometry of the fracture network, where most of the water flow occurs. The water flow in fractures is thus  
82 not uniform but occurs along preferential flow paths sometimes called “fingers” (Su et al., 2000), that channel the flow path  
83 at the larger scale of the fractured medium (Tsang et al., 2013). These preferential flow paths have been observed in both  
84 saturated and unsaturated fractures (Su et al., 2000).

85 In the study area of the Mont-Blanc massif, the fracture network opening is highly irregular (from millimeters to decimeters,  
86 depending on the fractures) and is expected to evolve seasonally, with reversible opening in winter (Guillet et al., 2018),  
87 superimposed on an irreversible long-term opening trend (Weber et al., 2017). The fractures can also be affected by the water  
88 flow, which can change the extent of ice filling or plugging and develop partially saturated conditions similar to those known  
89 from some epikarsts (Ford and Williams, 1989).

90 This study is motivated by the need to better understand hydrological processes in high mountain permafrost environments  
91 and connectivity with changing surface conditions, particularly in the context of ongoing climate change. We aim to address

92 major knowledge gaps in the hydrology of high-elevation permafrost rock regarding the timing, quantity, and source of water  
93 flow in the fractures, and how the flow is affected by surface conditions and the source of infiltrating water.

## 94 2. Study site and meteorological context

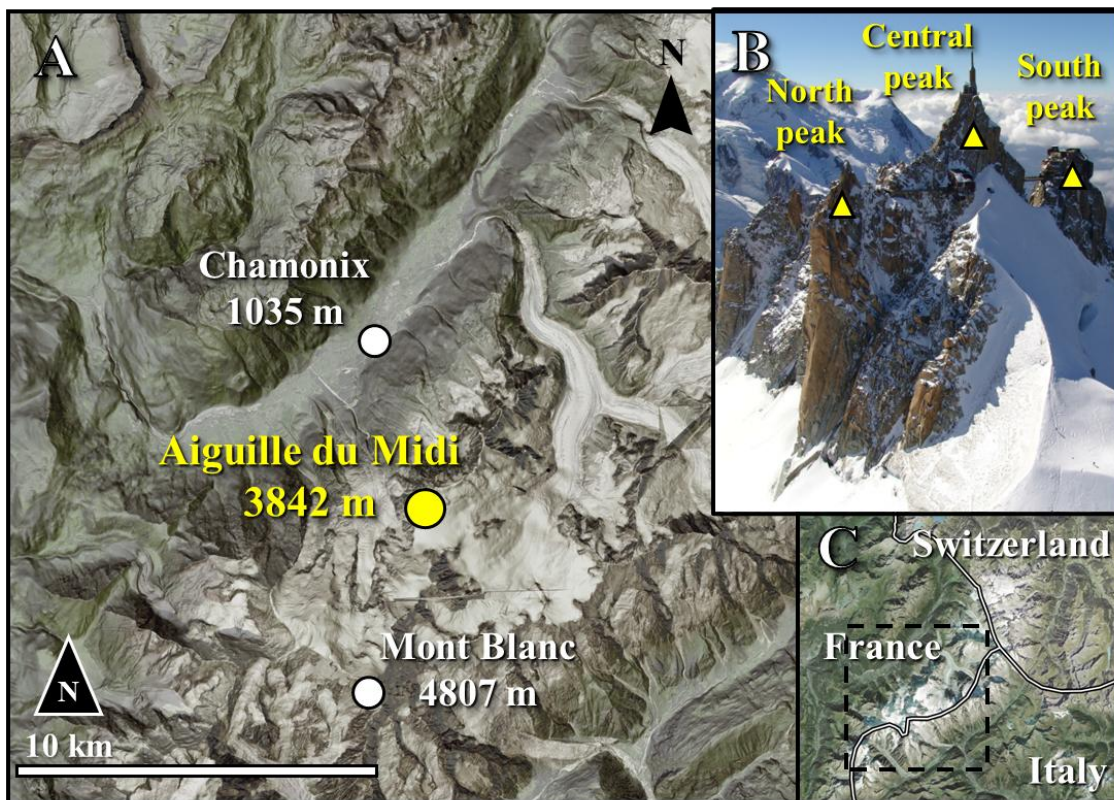
### 95 2.1. Aiguille du Midi site

96 The Aiguille du Midi (AdM) is a peak composed of three granite pillars - Piton Nord, Piton Central, and Piton Sud. The central  
97 pillar (Piton Central) reaches an elevation of 3842 m a.s.l and towers approximately 3000 m above the valley of Chamonix  
98 (Figure 1). The site lies on the NW flank of the Mont Blanc massif (MBM) which covers an area of about 550 km<sup>2</sup> and is  
99 oriented NW-SE between France, Italy, and Switzerland.

100 Glaciers occupied about 100 km<sup>2</sup> in the late 2000s (Gardent et al., 2014) while permafrost is largely present above  
101 approximately 2600 m in N faces and 3200 m in S faces (Magnin et al., 2015a).

102 The combination of steepness, permafrost, and glacial dynamics results in highly active morphodynamics (Deline et al., 2015).  
103 Over the past decades, rockfall ( volume > 100 m<sup>3</sup>) frequency has significantly increased (Ravanel and Deline, 2011), notably  
104 during the hot summers. The main cause has been suggested to be permafrost degradation (Ravanel et al., 2017; Legay et al.,  
105 2021; Magnin et al., 2023). Permafrost investigation started in the mid-2000s in the MBM, with the installation of various  
106 temperature sensors in AdM (Magnin et al., 2015b), including 10-m deep boreholes, which recorded a temperature increase of  
107 over 1 °C during the 2011-2020 decade (Magnin et al., 2024).

108 AdM has been chosen as a pilot site for alpine permafrost investigations because of its representativeness of high alpine  
109 rockwalls and its accessibility from Chamonix by a cable-car. Man-made tunnels, terraces, bridges, and an elevator allow the  
110 visitors to access different parts of the site. Since the hot summer of 2015, water flowing from the fractured tunnel walls has  
111 become a problem for the operating company (the *Compagnie du Mont Blanc*), leading to the installation of a drained metal  
112 plate ceiling to divert the flowing water and keep some parts of the tunnels dry for visitors.



113  
 114 **Figure 1:** A) Location of the Aiguille du Midi in the Mont Blanc massif. B) view of the three peaks at Aiguille du Midi. (Picture: S.  
 115 Gruber). C) Location of the Mont Blanc massif on the border of France, Italy and Switzerland. Maps provided by the Swiss Federal  
 116 Office of Topography swisstopo.

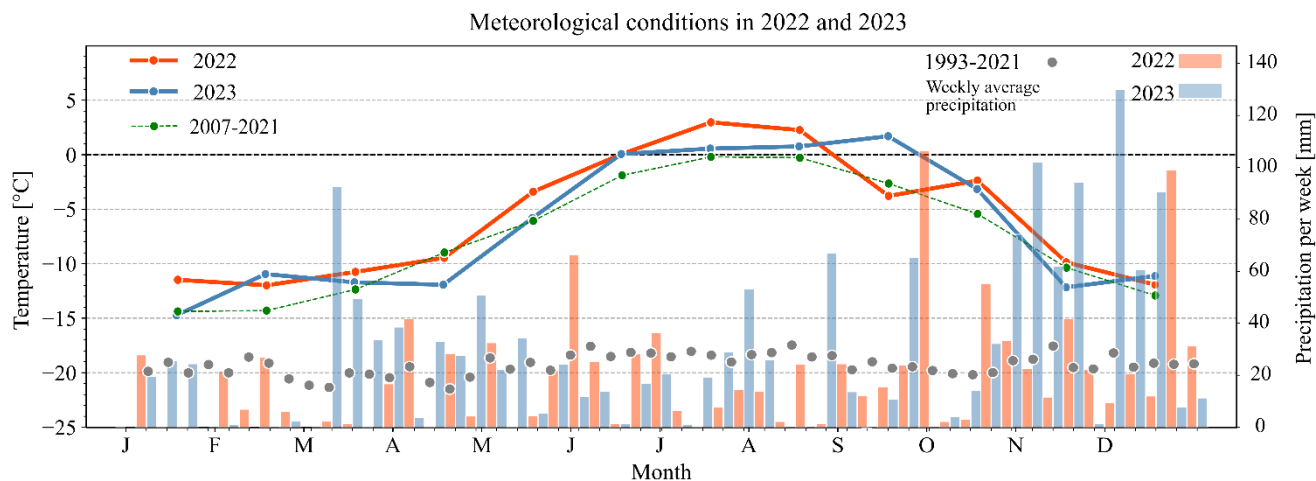
117 **2.2. Meteorological conditions in 2022 and 2023**

118 As of 2024, in Europe, the years 2022 and 2023 were the third and second warmest years in record after 2020, respectively,  
 119 with a mean annual air temperature (MAAT) about 1.1 °C above the 1991–2020 average (ESOTC 2023, 2024). Summer 2022  
 120 was the warmest summer ever recorded, outpacing the 1991–2020 average by 1.4°C (ESOTC, 2023). September 2023 was the  
 121 warmest September on record (EOSTC, 2023).

122 Air temperature (AT) and precipitation records in the town of Chamonix (France), located in the valley just north of AdM  
 123 (Fig. 1), began in the early 20<sup>th</sup> century and are well-suited to characterize the local precipitation regime. At AdM, AT records  
 124 started in 2007 but are affected by numerous gaps that sometimes last several months, making this data less reliable for multi-  
 125 annual comparison.

126 Figure 2 shows AT and precipitation in Chamonix and at AdM for 2022–2023. Winter and early spring 2022 were  
 127 markedly warmer and drier than in 2023, with mean AT at AdM about 1.4 °C higher and precipitation roughly half as much.

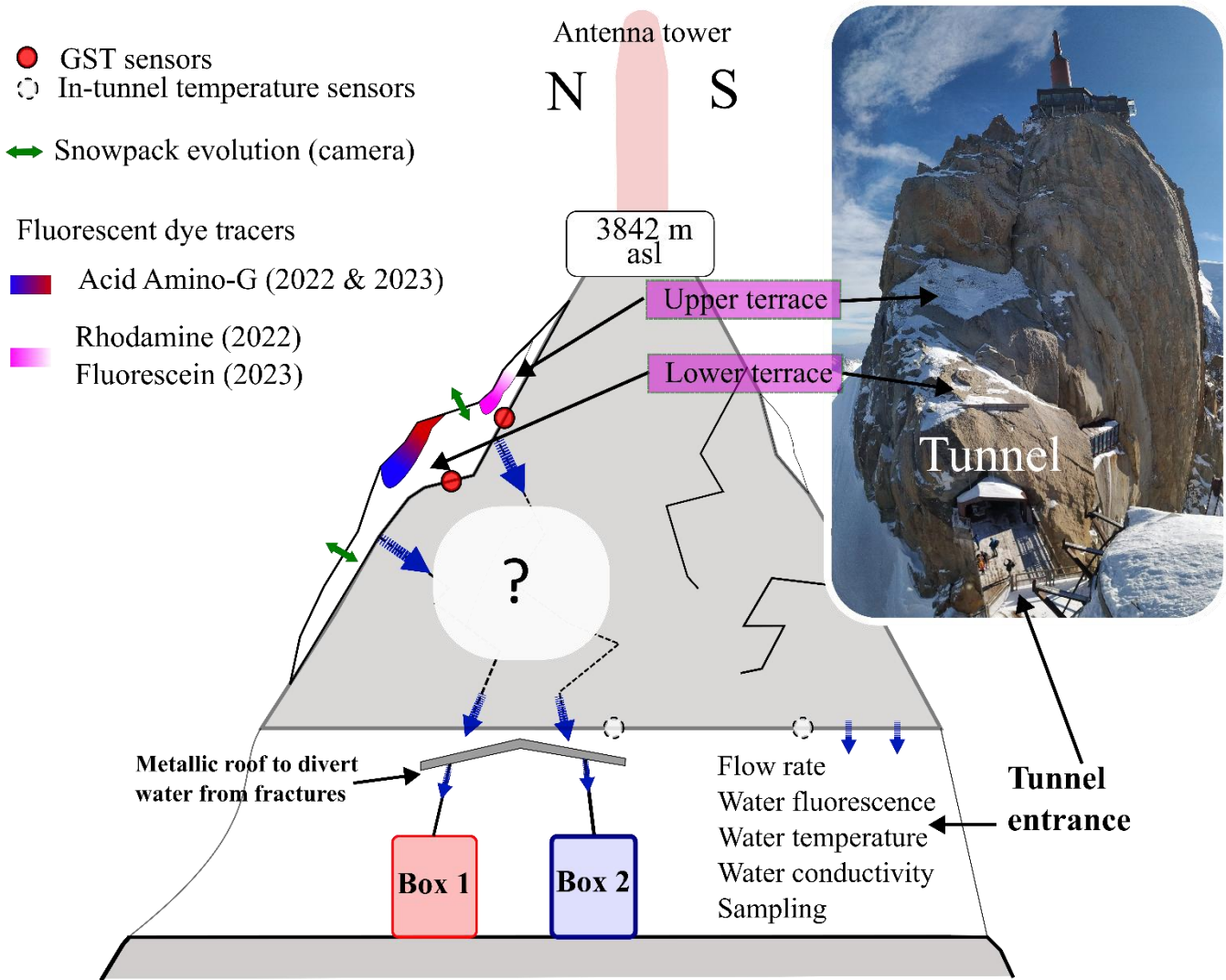
128 A late-spring heat wave produced a record high AT in May 2022, while May 2023 was near average. Summer conditions were  
 129 generally warmer in 2022, but an exceptional late-season heat wave occurred in September 2023—the warmest on record in  
 130 Chamonix—whereas September 2022 was near normal. Overall, 2023 was wetter than 2022, mainly due to higher precipitation  
 131 in spring and autumn.  
 132 In summary, 2022 was characterized by a very early but long-lasting and record-breaking summer heat wave, while 2023 was  
 133 characterized by a late and record-breaking summer heat wave with significantly more precipitation than in 2022.  
 134



135  
 136 **Figure 2: Monthly average air temperatures (Lines) and weekly precipitation (bars) in 2022 (orange) and 2023 (blue). Air**  
 137 **temperature was measured at the site in Aiguille du Midi (3842 m a.s.l). Precipitation was measured in Chamonix (1042 m a.s.l),**  
 138 **since no reliable precipitation data is available at the high elevation site. Data provided by Météo France. The long-term average**  
 139 **air temperature (2007-2021) is presented as a green thin dashed line. The long-term average weekly precipitation in Chamonix**  
 140 **(1993-2021) is shown by gray circles.**

141 **3. Methods**

142 In April and May 2022, we installed a monitoring system to measure characteristics of water flowing through fractures in the  
 143 roof of the tunnel in AdM (Figure 3, Figure 4).



144

145 **Figure 3: Sketch of the methodological approach to track and monitor water flows in the Aiguille du Midi central pillar. Note the**  
 146 **location of the insertion of the dye tracers in the snowpacks on the terraces above the water monitoring boxes.**

147

### 3.1. Fluorescent dyes in the snowpack

148

Fluorescent dyes were inserted into the snowpack at the surface above the tunnel in two locations, directly above the fractures (Figure 3), to trace the water source and rate of infiltration. In the 2022 season, two dye solutions were used: 20 L of sulphorhodamine-B solution with a concentration of 0.001 g/L and 20 L of amino acid G with a concentration of 20 g/L. These solutions were prepared and carried in “Ondine®” mineral water bottles by inserting the dye powders directly into the original mineral water, each with a volume of 5 L. The relatively low concentration of sulphorhodamine-B was chosen to have a light but detectable pink color, far above the detection limit of the fluorimeter sensor.

153

154 In 2023, new solutions were prepared in the same manner, using 1.5 L bottles of “Ondine®” mineral water. Sulphorhodamine-  
155 B was replaced by fluorescein dye, a much more soluble and detectable dye, to avoid confusion with sulphorhodamine-B from  
156 the previous year. In total, 9 L of fluorescein solution with a concentration of 0.667 g/L and 16 L of amino acid G with a  
157 concentration of 12.5 g/L were prepared.

158 In both years of the study, tracers were injected into the snowpack at the same two locations on the north face of the central  
159 peak (Figure 3). Sulphorhodamine-B in 2022 and Fluorescein in 2023 were injected on the "upper" terrace of the face, which  
160 is located 18-24 meters above the tunnel, while amino acid G was injected on the "lower" terrace, 7-12 meters above the tunnel,  
161 in 2022 and 2023. The tracers were inserted in spring, before the flow started: on the 11 May 2022 and 22 March 2023. We  
162 poured the solution in 5-10 points on each terrace and on the snowpack surface.

### 163 3.2. Ground surface temperature at the snow-rock interface

164 Four miniature temperature sensors (iButtons, Mouser®) have been installed in holes drilled 5 cm into the rock surface, at the  
165 snow-rock interface, on the terraces where the fluorescent dyes were injected. The holes containing the coin-sized sensors  
166 were filled with gray polymer clay to insulate the metal sensors from direct solar radiation. The sensors monitored GST at  
167 hourly time steps and over different periods (Table 1 **Error! Reference source not found.**), but only one (#61B8) monitored  
168 the temperatures during both seasons.

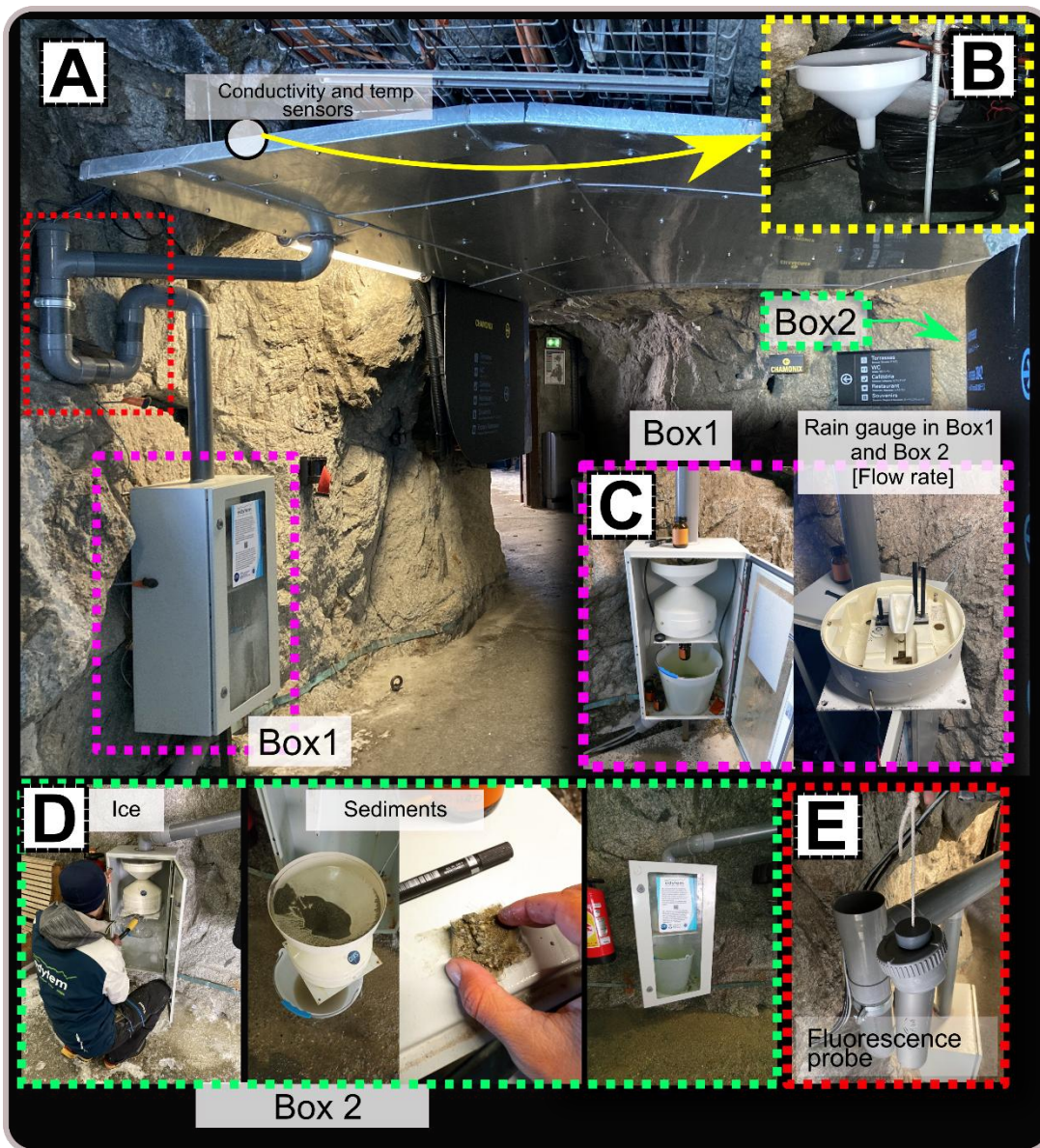
Sensor ID	Monitoring period covered	Location on the face
7077	11/05/2022 to 23/09/2022	In drilled hole at base of vertical rock outcrop
6202	06/09/2022 to 22/08/2023	In drilled hole at the surface of the lower terrace
608D	11/05/2022 to 22/08/2023	In a hole drilled at the base of a rock outcrop above the lower terrace
61B8	22/09/2022 to 22/08/2023	In the rock crack (same rock as 608D)

169 **Table 1: Miniature temperature sensors (‘iButtons’) at the snow-rock interface**

170 Snow melting was identified as “zero-curtain” periods in GST (Figure 5). These periods are characterized by stagnant GST at  
171 ~0 °C (Hanson and Hoelzle, 2004; Staub and Delaloye, 2017). The complete melting of the snow is marked by the transition  
172 from dampened GST daily oscillations to positive and significant daily oscillations once the insulating snow layer has melted  
173 and solar radiation reaches the rock surface. As GST is measured at point-scale, it lacks spatial representativeness of the snow  
174 melting surface area. Thus, to complete this data, pictures were frequently taken during fieldwork in 2022 to document snow  
175 patch evolution. In 2023, an automatic camera was installed (Figure 5) on a terrace of the North Pillar (See location on Figure  
176 1). From 1 March 2023 to 22 August 2023, it took 4 pictures a day of the north face of the Central Pillar, to monitor the snow  
177 patch evolution right above the water collection system. Pictures after 22 August 2023 are not usable because the protective  
178 glass was broken, and the pictures became blurred.

179 **3.3. Water flows and temperature monitoring in the tunnel**

180 We installed a real-time monitoring system in May 2022 in the west tunnel of the Central Pillar, to characterize the water  
181 flowing from fractures that cross the tunnel walls. We took advantage of an existing water diversion ceiling set up by the  
182 operating company (Figure 4), made of a convex metallic plate that collects water drips and flows, and diverts them to two  
183 pipes, one on each side of the tunnel (east and west) to drain water outside. Preliminary observations revealed that water was  
184 mostly dripping from two adjacent fracture systems with a generally subvertical dip ( $70^{\circ}$ - $90^{\circ}$ ) oriented toward north-west.  
185 The instrumentation included two rain gauges that were installed on each pipe to measure water flow rate (L/h), in protective  
186 boxes (Box 1 on the west side and Box 2 on the east side). Water temperature ( $^{\circ}$ C) and electrical conductivity (S/cm) were  
187 also monitored with sensors placed on the metallic roof, below the identified water drips. The sensors were submerged in a  
188 specially designed, 3D printed, siphon-shaped pipe (Figure 4B) to maintain a high water exchange rate and a minimal water  
189 level for detection. As a conductivity benchmark, we measured a value of  $9.2 \mu\text{S/cm}$  from a melted snow sample collected on  
190 the 26 July 2023, which corresponds with known values for snowmelt samples (Brennan et al., 2020; Thompson et al., 2016).  
191 In addition, water fluorescence (arbitrary units) was monitored in real-time with a probe inserted in Box 1 to detect the specific  
192 emission spectrum of the dye tracer used: Amino-acid-G and sulphorhodamine-B in 2022 and Amino-acid-G and Fluorescein  
193 in 2023 (see Sect. 3.1 for dye spraying strategy). The fluorescence sensor installed in 2022 (GGUN FL-24) malfunctioned  
194 during the 2022 winter and was replaced by a new probe (STREAM model, TRAQUA<sup>®</sup>) on the 31 May 2023, and was  
195 removed on the 22<sup>nd</sup> of August several weeks after the last dye signal was detected.  
196 Average values from the installed sensors were recorded every 10 minutes with a PC400 Campbell Scientific data logger. In  
197 addition, data from miniature temperature sensors (iButtons, Mouser<sup>®</sup>) that were previously installed were used to monitor  
198 the tunnel wall (bedrock) temperature.  
199 The site was visited weekly ,excluding a short period from 25 July 2023 to 10 August 2023 because of a storm that prevented  
200 access, to retrieve data, take water samples and manual measurements on electrical conductivity, and to clean the rain gauge,  
201 since sediments sometimes accumulated (Figure 4).



202  
203  
204  
205  
206  
207

**Figure 4: Real-time monitoring system in the tunnel. A) The metal roof and Box 1 (pink dashed frame). B) A 3D printed siphon that was placed directly under the water output from the fracture, equipped with temperature and conductivity sensors (yellow dashed frame). C) Box 1 interior with rain gauge to monitor flow rate, a sampling bottle, and a bucket. D) Box 2 with sediments (green dashed frame). E) Fluorescence probe by TRAQUA located in a specially designed siphon for continuous real-time monitoring of the dye tracers.**

208

### 3.4. Water sampling in the tunnels and laboratory analysis

209

Water samples were collected weekly from Box 1 during the melting seasons of both 2022 and 2023. Other locations in the tunnel (labeled Box 2 and TNL) were sampled occasionally in 2022 and weekly in 2023. Samples were taken in 125 mL brown

210

211 glass bottles. During the 2023 season, the electrical conductivity of each sample was measured directly after collection. The  
212 bottles were stored in a fridge to minimize biological activity and protect them from light.  
213 Further high-resolution fluorescence analysis of the water samples was carried out in a laboratory, using a fluorescence  
214 spectrophotometer (Varian Cary Eclipse) to validate the real-time fluorimeter data. The samples were exposed to light whose  
215 wavelength spectrum matched the excitation spectrum of the dye tracers used in the experiment. The emission vs. excitation  
216 wavelength plots were used to find peaks in emission distribution that corresponded to the presence of the dye tracers.  
217 In addition to fluorescence analysis, we performed stable isotope analysis on 11 water samples to determine  $\delta^{18}\text{O}$  and  $\delta\text{D}$   
218 values. Stable isotopes are widely used in hydrological studies to trace the origin and history of water, as their ratios are  
219 sensitive to fractionation during phase changes in the hydrological cycle. Such analyses can reveal important information about  
220 water sources (e.g. snowmelt vs. rainfall), transport pathways, and storage times. By comparing the measured isotopic  
221 signatures to the Global Meteoric Water Line (GMWL), we can assess whether the water follows typical meteoric patterns or  
222 has undergone secondary processes such as evaporation, mixing, or prolonged subsurface residence. Deviations from the  
223 GMWL can also indicate elevation effects or seasonal variations in precipitation, making isotope data a valuable complement  
224 to physical and chemical tracers in characterizing alpine hydrological systems.

### 225 **3.5. Data analysis**

226 We processed and analyzed the continuous time series data by developing codes in Python3 and MATLAB. All time series  
227 were filtered for erroneous values and interpolated to evenly spaced time steps for consistency.

#### 228 **3.5.1. Recession curves analysis**

229 Recession curves have been studied since the late 19<sup>th</sup> century (Brutsaert and Nieber, 1977; Tallaksen, 1995) and are commonly  
230 used in hydrology to interpret the flow behavior and characteristics of aquifers. A key advantage of this approach is that it  
231 allows the derivation of empirical, quantitative parameters that reflect the subsurface drainage. Following work by Boussinesq  
232 (1877), Maillet (1905) suggested an exponential analytical solution to describe aquifer drainage behavior:

$$233 \quad Q(t) = Q_0 e^{-at}, \quad (1)$$

234 where  $Q$  is flow rate,  $t$  is time,  $Q_0$  is peak flow rate, and  $a$  is the recession coefficient. To account for flood recession in a  
235 channelized flow, we opted for the general form suggested by Brutsaert and Nieber (1977) that is commonly used for river  
236 flood recessions (Brutsaert and Nieber, 1977; Krakauer and Temimi, 2011):

$$237 \quad \frac{dQ}{dt} = -aQ^b, \quad (2)$$

238 which can be integrated and solved for  $Q(t)$  as:

$$239 \quad Q(t) = (Q_0^{1-b} - a(1-b)t)^{\frac{1}{1-b}}, \quad (3)$$

240

241 where  $a$  and  $b$  are constant coefficients. Note that the integration of Equation 2 in the case of  $b=1$  corresponds to the form of  
242 exponential decay as expressed by Equation 1. Scandroglio et al. (2025) recently applied Maillet’s law (Equation 1) to analyze  
243 flow in fractures within a permafrost-affected rock wall in the Northern Calcareous Alps, at the German-Austrian border. Their  
244 study focused on a 55 m-deep tunnel in karst limestones, where flow paths extend at least 55 m and possibly farther due to  
245 tortuosity. In contrast, in our study, flow is confined to widely open, sub-vertical granite fractures with path lengths ranging  
246 from 12 m (lower terrace) to 20 m (upper terrace). Additionally, while we define a flow event as the period between a well-  
247 defined rise and the following recession of the hydrograph, Scandroglio et al. (2025) defined an event as a flow period  
248 beginning with a sudden increase in discharge, independent of the starting value, and ending when the flow returns below a  
249 set threshold, potentially including several peaks. They applied a single best-fit curve to their entire dataset, which comprised  
250 23 such high-flow events over eight years. Their approach is well suited to rain-controlled conditions. In contrast, our field  
251 site at 3840 m a.s.l. is dominated by snowmelt and thus strongly influenced by the diurnal solar cycle. We therefore identified  
252 93 well-defined single-peak events for recession-curve analysis over two consecutive seasons. To capture temporal variations  
253 in flow characteristics, we developed an automated algorithm that fits a separate recession curve to each event, enabling to  
254 track changes in flow behavior over time (Figure S2, S4). For each event, the algorithm identifies the recession limb as the  
255 interval between the last local maximum and the subsequent return to baseflow. It then isolates the concave segment of this  
256 limb (curvature  $> 0$ ), which corresponds to the exponential decay, and fits the appropriate form of Eq. 1 or Eq. 2. To ensure  
257 that only well-defined exponential recessions are included, events with regression fits yielding  $R^2 < 0.8$  are discarded. This  
258 threshold retains 64% of all detected events (93 out of 144) while excluding cases where noisy or multi-peak recession behavior  
259 prevents reliable fitting.

### 260 **3.5.2. Moving window cross-correlation**

261 A moving-window cross-correlation analysis was performed to quantify the correlations and lag times between pairs of  
262 measured time series, including flow rate, AT, and GST. For each lag time, the Pearson correlation coefficient (PCC) was  
263 calculated between one series and a time-shifted version of the other (+1: high correlation, 0: no correlation, -1: reverse  
264 correlation). For example, at a lag time of 0, the flow and AT were measured at the same time; at a lag time of +6 h, the flow  
265 series was correlated with the AT series shifted forward by 6 h. Lag times were evaluated in the range of -12 to +12 h in steps  
266 of 1 h.

267 The analysis was performed in a moving window of 24 hours starting from 00:00, without overlapping, which corresponds to  
268 the observed daily cycles in both flow rate hydrograph, and GST and AT. Window size is an important parameter: shorter  
269 windows highlight transient events but may be sensitive to noise, whereas longer windows yield more stable estimates at the  
270 cost of smoothing short-term variability. In this study, a window length of 24 hours was selected as a compromise between  
271 detail and stability.

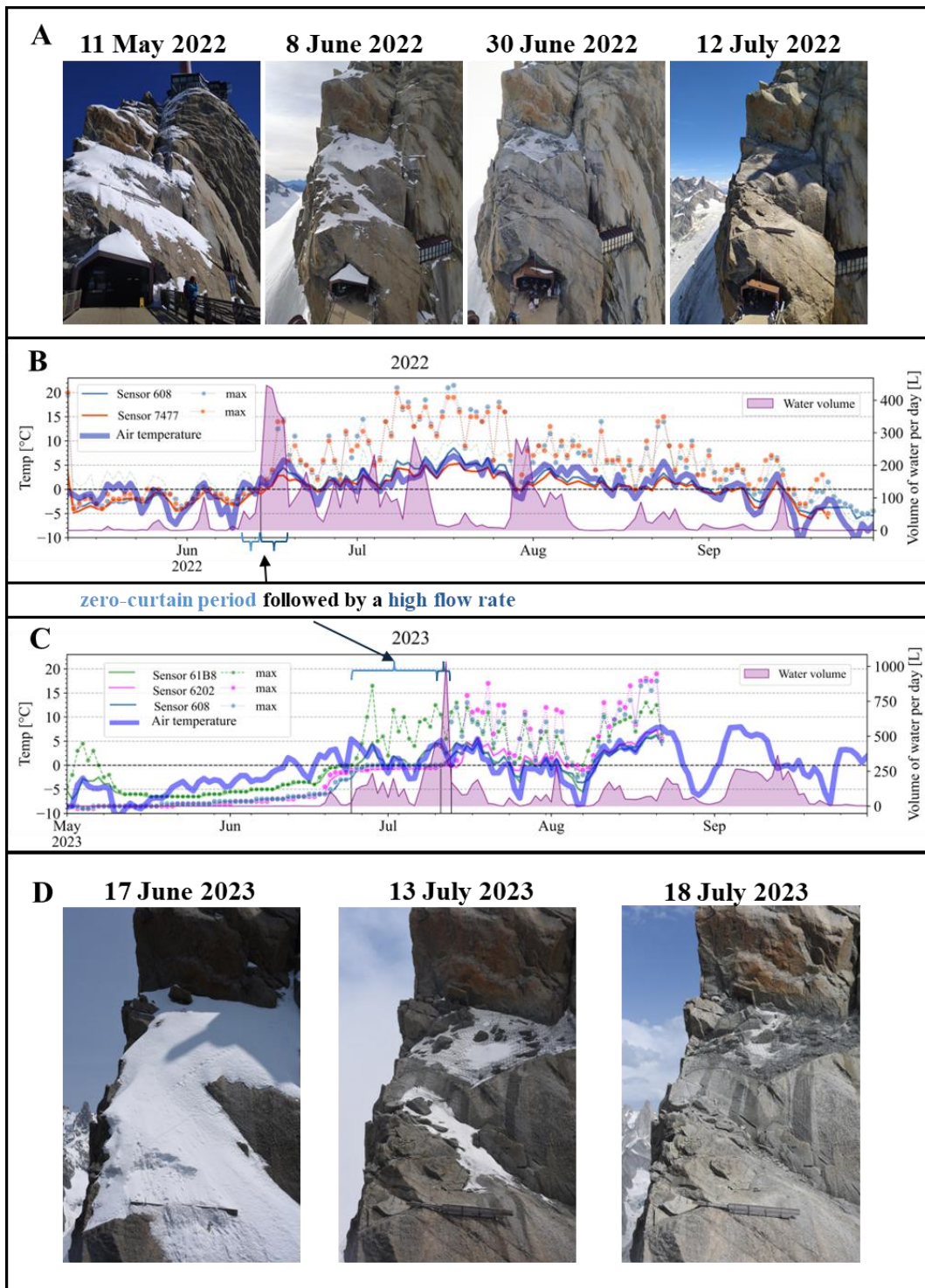
272 Prior to analysis, all time series were filtered with a one-hour moving average to reduce high-frequency noise. Only days with  
273 a maximum flow rate above  $6 \text{ L h}^{-1}$  were included, ensuring hydrographs with clear diurnal signals. The analysis was conducted  
274 over the entire flow season (mid-May to August in 2022, and June to September in 2023).

## 275 **4. Results**

### 276 **4.1. Water flow rate**

277 Water flow is highly seasonal. In both years, water mostly flowed between May and October, with periods of sporadic and  
278 continuous flow that can last several weeks. The occurrence of water flows correlates with the occurrence of positive AT  
279 (Figure 5).

280 In 2022, sustained periods of water flow were mainly observed from late May to mid-September, and in 2023, from mid-June  
281 to late September. The timing and magnitude of the flow differed between Box 1 and Box 2 (Figure 6). In both years, water  
282 flow in Box 1 began several weeks earlier than in Box 2. In general, the amount of water in Box 2 increased throughout the  
283 summer season.



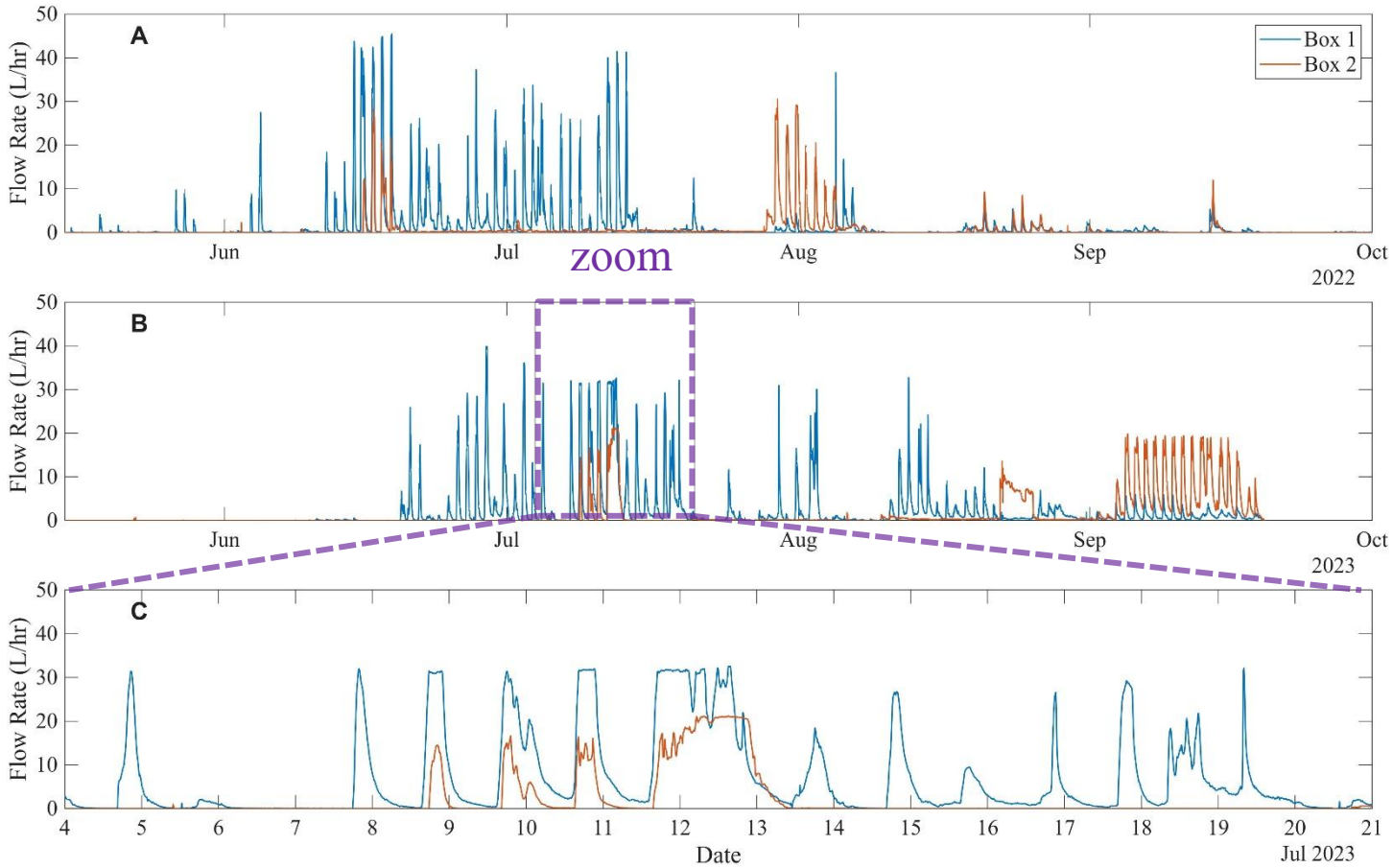
284

285

286

**Figure 5:** A) Photos showing the evolution of the snow cover on the NE face during the snow melt season in 2022. B) and C) AT, GST measured on the NE face, above the tunnel entrance, directly above the monitoring system, and flow rate measured at the output

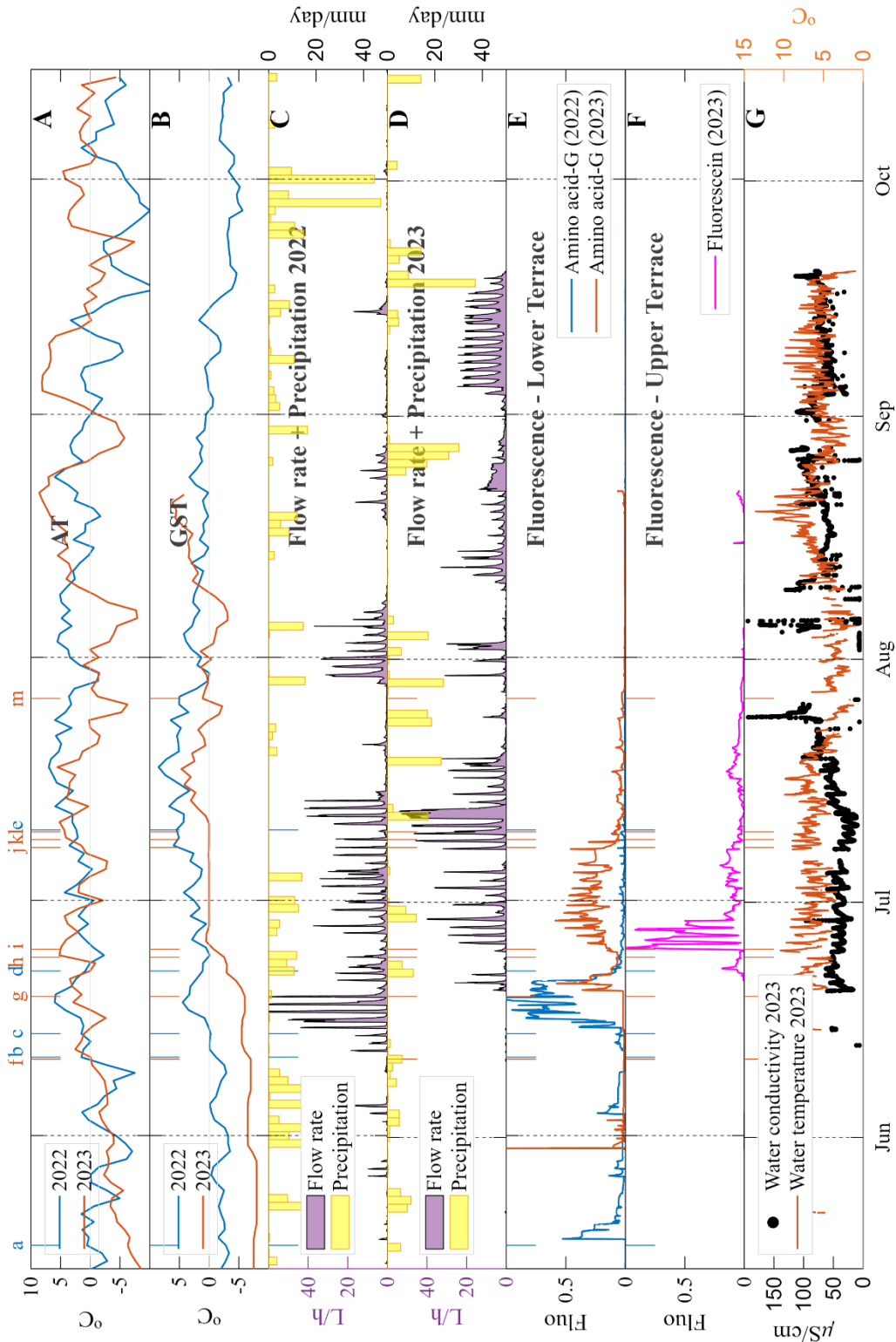
287 from rock fractures in the tunnel wall (Box 1+Box 2) in 2022 and 2023, respectively. Solid lines represent the daily average. Note the  
 288 zero-curtain period, which marks the melting of the snowpack and the exposure of the rock surface to atmospheric heating. D)  
 289 Photos showing the evolution of the snow cover on the NE face during the snow melt season in 2023.



290  
 291 **Figure 6: A) and B) Time series of flow rate in Box 1 (blue) and Box 2 (orange) during the 2022 and 2023 melt seasons, respectively.**  
 292 **C) Zoom window on the 4-21 July 2023 period.**

293 **In 2022**, the total volume of water flowing through the monitoring system (Boxes 1 and 2) was 8001 L. About 70% of this  
 294 volume (5621 L) was collected in Box 1, while the remaining 30% (2380 L) reached Box 2. 75% of the total volume in Box 1  
 295 occurred between 11 June and 14 July (4216 L). Of the total flow volume in Box 2, 74% flowed in two relatively short periods:  
 296 14 - 19 June (496 L) and 28 July - 8 August (1257 L).

297 **In 2023**, the total volume of water flow was 11605 L - 45% more than in 2022. Of this, 61% (7079 L) flowed through Box 1,  
 298 and 39% (4526 L) in Box 2. 75% of the total volume in Box 1 occurred between 19 June and 10 August (5309 L). In Box 2,  
 299 almost the entire volume (95%) flowed in three relatively short periods (3 to 18 days): 8 - 13 July (831 L), 22 - 25 August  
 300 (611 L) and 1 - 18 September (2851 L).



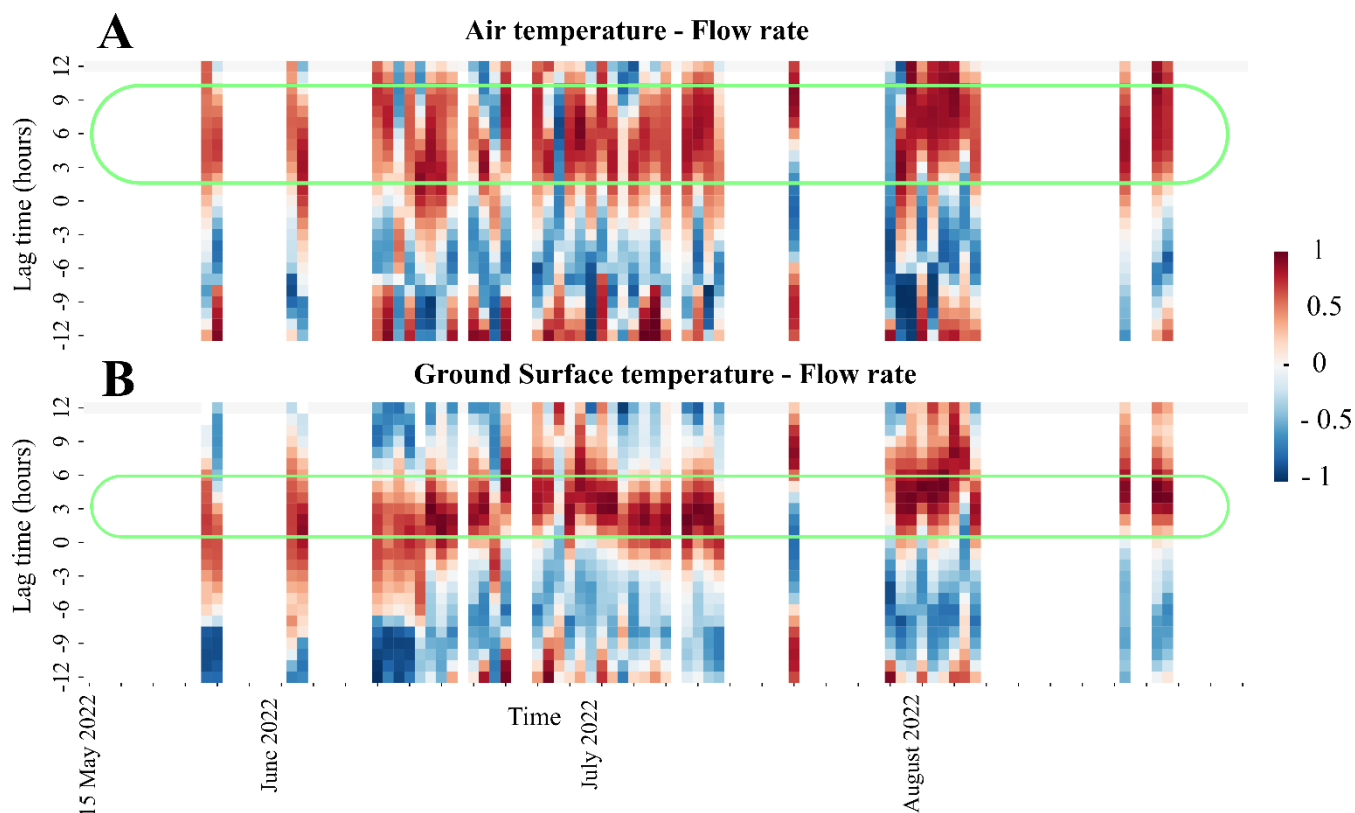
302 **Figure 7: Annual time series. A) Air temperature (AT) measured by Météo-France in Aiguille du Midi. B) Ground surface**  
 303 **temperatures (GST) measured using iButtons at the rock surface on rock slope. C-D) Flow rate measured in both box 1 + box 2**  
 304 **(purple) and daily precipitation measured in Chamonix meteorological station (Météo-France) (yellow bars). E) Normalized**  
 305 **fluorescence signal of amino acid-G dye tracer (2022 and 2023). F) Normalized fluorescence signal of Sulphorhodamins-B (inserted**  
 306 **in 2022) and Fluorescein (inserted in 2023) dye tracers. The Sulphorhodamins-B dye was never detected. G) Water conductivity and**  
 307 **temperature at the outlet of water from the fracture in the tunnel. Measurements in time steps without water flow were omitted**  
 308 **from the plot. Labeled annotation at the top of panel A mark the following main events in 2022 (blue): a) first flow event in box 1,**  
 309 **b) AT surpasses 0° C, c) GST surpasses 0° C + beginning of daily oscillations + first flow in box 2, d) amino acid G signal diminishes,**  
 310 **e) last amino acid G signal, and 2023 (orange): f) AT surpasses 0° C, g) first water flow event in box 1, h) beginning of daily**  
 311 **oscillations, i) beginning of zero curtain, j) first flow in box 2, k) amino acid G signal diminishes, l) end of zero curtain, m) last amino**  
 312 **acid G signal.**

313 The observed flow rate presents daily cycles (Figure 6) with peak flow rates, reaching an order of  $10^1$  L/h, generally occurring  
 314 between 17:00 to 20:00 (Table 2, Figure S1), and minimum flow rates two orders of magnitude lower (order of  $10^{-1}$  L/h) during  
 315 the morning time.

	Average time of signal peak	
	2022	2023
<i>Air temperature (AT)</i>	12:00-15:00	11:00-15:00
<i>Ground surface temperature (GST)</i>	15:30-18:00	15:30-17:00
<i>Flow rate</i>	18:00-19:50	16:20-20:30

316 **Table 2: Time of day of the daily peak in flow rate, AT, and GST. The listed time ranges represent the 25–75% quantile of daily**  
 317 **peak timing**

318 Results of a moving window cross-correlation show that daily flow rate oscillations are correlated with AT with a lag time of  
 319 3-9 hours, and with GST with a lag time of 0-6 hours. This lag time was found to be steady in both years of the experiment  
 320 (Table 2, Figure 8).



321

322 **Figure 8: Results of moving-window cross-correlation analysis between the water flow rate and the (A) air temperature and (B) the**  
 323 **ground surface temperature, during 2022 season. The horizontal axis represents the time (one strip per day), and the vertical axis**  
 324 **represents the lag time, in hours. The color bar represents the value of the Pearson correlation coefficient (PCC) (1: high correlation,**  
 325 **0: no correlation, -1: reverse correlation). The green frame marks the range of lag times that show high PCC. Results of the cross-**  
 326 **correlation analysis of 2023 season show similar results and can be found in the supplementary materials, in figure S3.**

327 In 2022, the first flow in Box 1 was recorded on 15 May (1.1 L/h) and gradually increased, reaching continuous daily flows  
 328 with peak values larger than 40 L/h from 11 June to 14 July, after which flows were linked to rainfall. Box 2 showed its first  
 329 significant flow (>10 L/h) on 15 June, with continuous daily oscillations lagging about 5 days behind Box 1. Maximum flow  
 330 rates were 45 L/h in Box 1 and 30 L/h in Box 2, with a combined peak of 67 L/h on 16 June.

331 In 2023, Box 1 exhibited continuous daily oscillations from 19 June, peaking at 40 L/h on 28 June, interrupted by short cold  
 332 spells, and resuming under positive AT and precipitation events (Figure 6). Box 2 began daily flows between 8–13 July (up to  
 333 20 L/h) with a prolonged steady flow (5–12 L/h) from 22–25 August despite minimal precipitation. Maximum individual flows  
 334 were 39.83 L/h in Box 1 and 21.20 L/h in Box 2, with combined peak flow of 54 L/h on 12 July. Daily maximum volumes  
 335 reached 446 L in 2022 and 1033 L in 2023 (Figure 6).

336

---

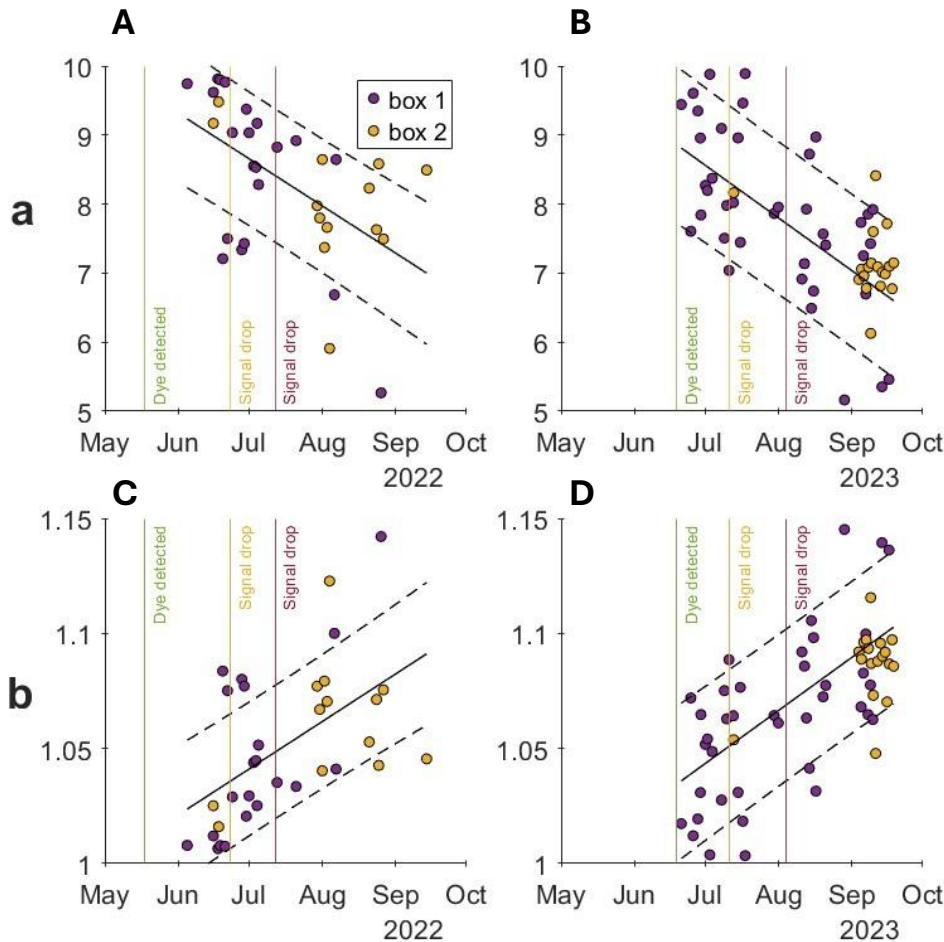
**Peak flow rate (L/h)**

---

	Box 1	Box 2	Daily max volume (L)
<b>2022</b>	45.4	30.5	446
<b>2023</b>	39.8	21.2	1033

337 **Table 3: Flow rates peaks**

338 The exponential recession curves (Eq.1) fit well with the observed daily events, with an average  $R^2$  value of 0.93. Curves with  
339  $R^2$  values below 0.8 were omitted from the analysis, resulting in 93 events (Figure 9). The ‘a’ coefficient shows a clear  
340 decreasing trend in time from values of 7-10 to 5-8.5 in both 2022 and 2023 seasons (Figure 9), while the ‘b’ coefficient  
341 increases from values of  $b \approx 1$  at the beginning of the melting season to values of  $b \approx 1.15$  at the end of the season (Equations 2  
342 and 3).



343

344 **Figure 9: A-B) values of the ‘a’ coefficient of the recession curves of flow events in 2022 and 2023 in box 1 (purple circles) and box**  
345 **2 (yellow circles). C-D) values of the ‘b’ coefficient of the recession curves of flow events in 2022 and 2023 in box 1 (purple circles)**  
346 **and box 2 (yellow circles). Values obtained from curves with  $R^2$  values below 0.8 were omitted from the analysis. The black line is the**

347 **linear regression of all the points (box 1 + box 2) with  $\pm$ standard error (dashed black lines). The vertical lines indicate the timing of**  
348 **the detection of the fluorescent dye in the water that exits the fractures (green), the rapid drop of the signal intensity (orange), and**  
349 **the disappearance of the signal (red).**

350

## 351 **4.2. Snowpack evolution and water flow characteristics**

352 Snowpack evolution is assessed through GST measurements at the snow-rock interface and using time-lapse pictures in 2023.  
353 Dampened daily oscillations in GST indicate the presence of a snowpack with a significant insulating effect. The melting period  
354 is generally visible as a zero-curtain period (*i.e.* persisting 0 °C conditions at the rock-snow interface) (Hanson and Hoelzle,  
355 2004) that lasts from several days to several weeks.

356 Figure 5 displays the measured GST data at the rock-snow interface Figure 5. In 2022, the dampened daily oscillations are  
357 revealed by the similar values of mean and maximum GST, and the zero-curtain period is nearly nonexistent. This could be  
358 related to the early heat wave in 2022 that accelerated snow melting. Nonetheless, the first water flow events in May and early  
359 June 2022 occurred when GST rose close to 0 °C, demonstrating a link with snow melting. The first significant water flow  
360 event in 2022, which is also the greatest one with values reaching over 400 L/day, coincides with the transition to positive  
361 GST around mid-June. Summer precipitation episodes are suggested when water flow events follow periods with limited water  
362 flow and positive GST and AT, such as in late July 2022. In 2023, the effect of snow cover on GST patterns is more evident,  
363 with an initial period of non-existent daily oscillations followed by a zero-curtain period until mid-July. The first flow events  
364 occurred during the onset of the snow melting period, with the highest peak of water flow reaching > 1000 L/day at the end of  
365 the zero-curtain period.

## 366 **4.3. Fluorescence**

### 367 **4.3.1. Real-time fluorescence monitoring**

368 In 2022, the real-time fluorescence sensor shows a strong signal of amino acid-G that followed the very first flow events in  
369 mid-May 2022 (Figure 7) and the sporadic flow events that followed it until 11 June 2022. The high amino acid-G signal  
370 continued with the onset of continuous water flows around mid-June 2022, until the rapid decrease at the end of June. The  
371 disappearance of the fluorescent signal, despite the sustained water flow likely corresponds to the complete melting of the  
372 lower terrace snowpack that contained the amino acid-G tracer, as seen in the photos from the time lapse camera (Figure 5).  
373 A weak signal of amino acid-G was detected until mid-July 2022 when both the fluorescence and flow rates diminished. This  
374 period of weak amino acid-G signal in the water could indicate dilution with water from precipitation that occurred after the  
375 dye was inserted or another not-dyed source (either late snow or rain). No signal of the sulphorhodamine-B tracer inserted in  
376 the upper ledge was found. This could be due to excess dilution of the tracer solution with the snowmelt water to concentrations

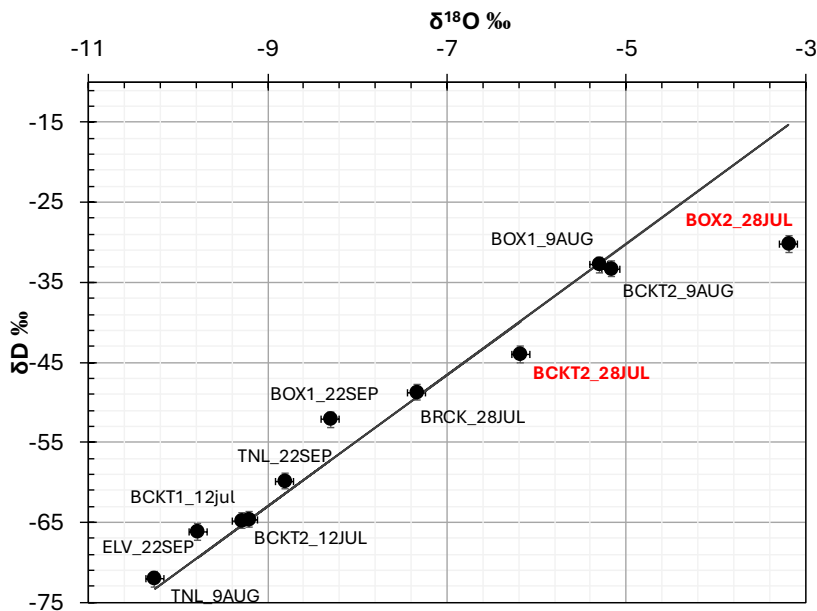
377 that were below the sensor sensitivity. A second hypothesis is that snowmelt from the upper terrace did not reach the fracture.  
378 In 2023, the amino acid-G signal was also detected in the first water flows on 19 June. From the 24 June 2023 onwards, the  
379 signal of the fluorescein dye was detected alongside amino acid-G, which likely confirms that the concentration in  
380 sulphorhodamine-B was probably too low in 2022. The fluorescein signal is shorter than the amino acid-G signal, with a single  
381 high peak in the last week of June followed by a rapid decrease to low values. This could be explained by the different pathways  
382 from the upper terrace snowpack through the fracture network, together with the effect of low dispersivity of fluorescein. The  
383 high peaks of amino acid-G persisted continuously until 8 July. Afterward, both tracers remained in low concentrations until  
384 the end of July, suggesting that much of the winter and spring snow had melted by 27 July. That could mean that the time  
385 needed for the entire winter snowpack to infiltrate is slightly more than a month. After that, the water flowing from mid- to  
386 late July was either direct precipitation (rain and snow) or possibly meltwater from ice that predated the tracer insertion.

#### 387 **4.3.2. Fluorescence laboratory results**

388 Additional analyses of water samples collected between May and mid-July 2023 from Boxes 1 and 2 and various fractures  
389 dripping into the tunnels of AdM were carried out using a high sensitivity spectrophotometer in the EDYTEM laboratory. The  
390 results are similar and confirm those found using the TRAQUA real-time sensor in Box 1. The signals for Fluorescein and  
391 amino-G show peaks at the same periods, i.e. at the end of the month of June and the beginning of July. The fluorescein signal  
392 is very short-lived, unlike amino-G, which continues to appear for a longer period. Samples from other locations in the tunnel  
393 show no signal of any of the fluorescent dyes.

#### 394 **4.4. Stable isotopes**

395 Analysis of oxygen and hydrogen isotopes in the water samples shows that  $\delta^{18}\text{O}$  and  $\delta\text{D}$  values range between -3.2‰ to -10‰  
396 and -15‰ to -73‰ respectively (Figure 10). Excluding two samples, the  $\delta^{18}\text{O}/\delta\text{D}$  ratio in all the water samples fall close to  
397 the global meteoric water line (GMWL) or align on a straight line parallel to the GMWL, likely because of a seasonal evolution  
398 of the local meteoric line from the GMWL (i.e. three samples taken on 22 September -labeled \_22SEP). Two samples taken  
399 on 28 July 2022 from Box 2 deviate significantly below the GMWL (BOX2\_28JUL – directly from the fracture,  
400 BCKT2\_28JUL – from a 5L bucket that collected the water from the fracture) (Figure 10). This suggests that the water  
401 emerging from the fracture above Box 2 on that day was not of recent meteoric origin.



402

403 **Figure 10: Stable isotopes  $\delta^{18}\text{O}$  and  $\delta\text{D}$  in water samples. Note the two outliers (labeled in red) from the global meteoric water line**  
 404 **(GMWL, black line) in samples taken from Box 2 on 28 July 2022.**

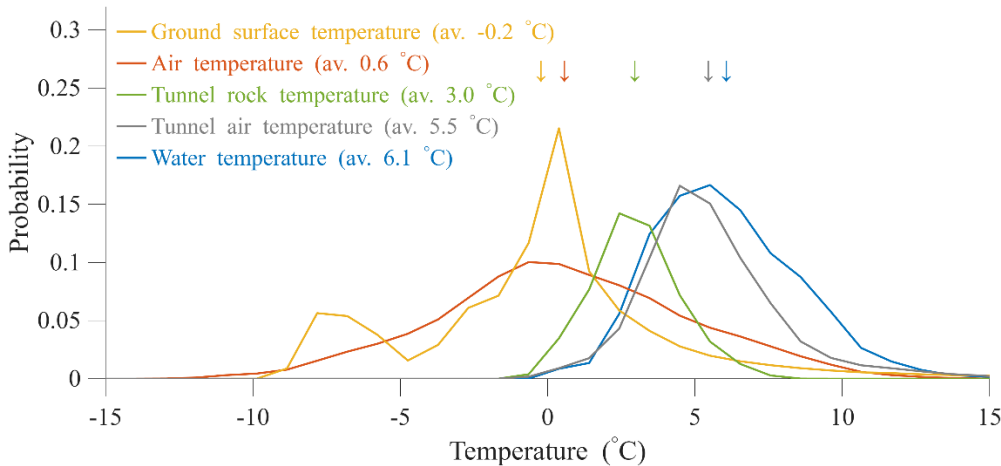
405

#### 4.5. Water electrical conductivity

406 Electrical conductivity values are provided as maximum values per day of flow, after correction to a standard temperature of  
 407 25°C. The electrical conductivity measurements from the 2022 season were unreliable due to the erroneous installation of the  
 408 sensor. Therefore, only the 2023 results are presented and analyzed (Figure 7). Overall, the conductivity values were far above  
 409 the benchmark value measured in melted snow samples (9.2  $\mu\text{S}/\text{cm}$ ). On the continuous measurement (real-time monitoring  
 410 system), the electrical conductivity of the water flowing into Box 1 remained relatively constant from mid-June to mid-July,  
 411 with daily oscillations between 10-55  $\mu\text{S}/\text{cm}$  and a general decreasing trend. The daily oscillations correlate with flow rate in  
 412 a reverse relation – when flow rate is high the conductivity decreases (Figure 7). These values of conductivity correspond to  
 413 the period of continuous cyclic flow rate in Box 1 that ended with the complete thaw of the winter snowpack. Interestingly,  
 414 significantly higher conductivities were measured at other locations in the tunnels. Conductivity measurements with values of  
 415 485  $\mu\text{S}/\text{cm}$  were taken in a tunnel wall under the west face of the central peak, from mid-July onwards, and 430  $\mu\text{S}/\text{cm}$   
 416 (measured in 2022) at another location in a tunnel under the north-east face of the central peak, near the exit of the cable car  
 417 going to Pointe Helbronner (Italy).

418 **4.6. Water temperature**

419 During flow events, the water temperature measured in two locations at outputs from the fractures ranges between 0 °C and  
420 13 °C with an average of 6.1 °C (Figure 11). Measurements taken during periods without flow or subzero temperatures were  
421 removed from the analysis. Average GST and AT during the thawing season (15 May to 15 September) are close to 0 °C.  
422 Values measured at the rock surface in the tunnel walls, near the fractures, during flow events show an intermediate mean  
423 value of 3.0 °C.



424 **Figure 11: Probability distribution of temperatures monitored during flow events (blue), atmospheric ATs (orange), ground surface**  
425 **temperatures (yellow), tunnel wall (green), and tunnel air. All distributions show data from the thawing season in 2022 and 2023 (15**  
426 **May – 15 September). Note that the water temperature distribution (blue) shows only data when water flow was detected in the**  
427 **monitoring system, while the other temperature distributions represent the entire data within the thawing season. The arrows show**  
428 **the location of the mean values on the horizontal axis.**  
429

430 **5. Discussion**

431 **5.1. Water flows and weather conditions**

432 Our results show rare evidence of highly effective surface-subsurface connectivity in steep permafrost-affected slopes, and  
433 strong weather signals in both seasonal and diurnal scales. There is a clear link between the timing of AT and GST becoming  
434 positive in the early summer months and the onset of water flow. The first flow events in the season, which appeared in early  
435 May (2022) and June (2023), display a clear signal of the dye tracer and are directly linked to snow melting occurring under  
436 positive AT in the relatively shaded north-exposed rock face.

437 In both years, the onset of water flow in the fractures occurred when the daytime AT reached values above 0 °C. This change  
438 in temperature to positive values directly induced the melting of the snow that was deposited during winter, and its infiltration  
439 into the fractures. The melting of the snowpack is demonstrated by the simultaneous detection of the fluorescent dye tracers  
440 injected into the snowpack and the zero-curtain effect observed in the GST (Figure 5, Figure 7). The melting accelerated when

441 the rock surface was exposed to heat flux from the atmosphere and GST turned positive. From this point onwards, water flow  
442 behavior became more uniform, with regular daily oscillations, and reached the highest flow rates. Subsequently, after the  
443 exposure of the rock surface, some of the water in the fracture was directly from precipitation, which likely melted rapidly on  
444 the rock surface as the temperature increased, often above 0 °C. Each year, water flow in the fractures ceased when the  
445 temperature became negative again in autumn, with icicles appearing in the fractures.

446 Based on the 2-year monitoring, we conclude that water flow processes in high mountain rock faces are therefore seasonal,  
447 directly linked to the change in air and surface temperatures to above 0 °C during the summer period and below 0 °C during  
448 fall. The continuous detection of the dye, together with an analysis of time-lapse photos of the rock face and the shift of GST  
449 to positive values, show that snowmelt is the main source of water in the fractures during the early and main stages of flow,  
450 and contributes most of the water. This is consistent with similar observations reported by Scandroglio et al. (2025).

451 GST and AT also control flow rate oscillations on a daily time scale and are cross-correlated with a lag time of 3-9 and 0-6  
452 hours, respectively (Table 2, Figure 8, Figure S3). These lag times provide an estimation of the time taken for water to travel  
453 through the fracture system, and allow a rough approximation of flow velocity on the order of ~10 m/hr.

454 The observed acceleration in flow rate coincides with the heating of the rock surface to above 0 °C and points to a top-down  
455 thawing of the active layer (i.e. the near-surface layer that freezes and thaws through summer).

456 Nevertheless, the time lag between surface signal and water flow as well as the thawing of the active layer must be cautiously  
457 considered as it is possibly influenced by the open-system of the tunnel causing an open flow path and a thermal shortcut  
458 allowing for bottom-up heat transfer. In addition, the touristic infrastructure and human presence can contribute to internal  
459 heat sources, including heating systems, the elevator motor, and body heat from visitors (Figure 11).

### 460 **5.1.1. Heat waves effect**

461 The contrast in summer conditions between 2022 and 2023 further illustrates the strong influence of weather conditions on the  
462 timing and characteristics of the water flow period (Sect. 2.2). This is well demonstrated by the effect of the early heat wave  
463 in spring 2022 that resulted in an early onset of water flows and the late heat wave in autumn 2023 that extended the water  
464 flow period much later in the season. The 2023 season was significantly wetter in terms of precipitation, and subsequently,  
465 more water flowed in the monitored fractures. However, comparing the monthly distribution of flow during the thawing season  
466 reveals that it was greatly influenced by the heat waves. Between May to mid-July, flow volume in 2022 was much higher  
467 than in the same period in 2023, as a result of the early and rapid thawing. Only in late August, did the total volume of water  
468 flow surpass that of 2022. This raises an interesting point for future research on the influence of early vs. late water infiltration  
469 in permafrost rocks and the impact on hillslope processes. Assuming that water that infiltrates later in the season is warmer  
470 than the rock mass, and the infiltration paths contain less ice, it can potentially accelerate permafrost degradation and  
471 thickening of the active layer.

472 Compared to the less extreme spring temperatures in 2023, the rapid thaw in 2022 is evident in the GST data and in the absence  
473 of a zero-curtain period, which is clearly observed in 2023 (Figure 5, Figure 7). We suggest that during the early heatwave in  
474 2022, there was less snow, the thawing was very rapid, and the latent heat was absorbed rapidly. This can be seen in Figure 5,  
475 which shows less snow cover in min-June 2022 in comparison with mid-June 2023, and a large volume of water immediately  
476 after GST turns positive.

## 477 **5.2. Water flow path conditions**

478 Our results also indicate that an effective pathway exists within the fracture network through which the water released by  
479 snowpack melt can infiltrate at the end of spring. The early detection of fluorescent dye in the first flow events suggests a  
480 relatively rapid transfer from the surface to the fractures. Furthermore, when flow ceases at the end of autumn and icicles form  
481 at the fracture outlet, the observed flow appears to be unsaturated. In such cases, the unsaturated flow is likely routed through  
482 preferential pathways within the fracture system, which in turn suggests that at least part of the network remains open and able  
483 to convey meltwater during the following spring. However, we cannot overrule the possibility that the man-made space of the  
484 tunnel contributed to the unsaturated conditions. In natural conditions, if undrained conditions occur, water could accumulate  
485 in the fractures, refreeze inside them, and seal them off. Artificial prevention of ice accumulation can inhibit fracture  
486 development through ice segregation and the related cryostatic pressure (Draebing et al., 2014; Draebing and Krautblatter,  
487 2019; Hales and Roering, 2007; Hallet et al., 1991; Matsuoka and Murton, 2008; Matsuoka and Sakai, 1999). Completing  
488 these water flow observations with crack-meters to measure fracture rheology would provide an interesting perspective to  
489 clarify the role of the tunnel. However, this would require to identify the fractures that are directly connected to the tunnel.  
490 Interestingly, our monitoring system shows different but consistent timing of water flows in Boxes 1 and 2, despite them being  
491 located only a few meters apart (Figure 6). One reason for the delayed flow in Box 2 could be linked to the location of the  
492 draining area closer to the colder north face, while the draining area of Box 1 is closer to the west face, which receives more  
493 solar radiation. Another explanation could be suggested based on the observed accumulation of sediments in Box 2, which  
494 was not observed in Box 1. The origin of the sand-size sediments observed in Box 2 is very likely from the erosion of the  
495 granite rock. This suggests that the fracture system drained to Box 2 is filled with sediments that reduce the hydraulic  
496 conductivity. However, once flow begins in Box 2, it responds directly to precipitation and positive AT and reaches high flow  
497 rates, similar to those measured in Box 1 (e.g. in September 2023, Figure 6, Figure 7). This supports the first hypothesis of  
498 different exposures to solar radiation. The effect of the sediments filling on the hydraulic conductivity is thus reduced in late  
499 summer, perhaps due to the thawing of ice-filled pores within the sediments filling. Alternatively, the sand and ice in the sub-  
500 vertical fractures might act as a partial plug that accumulates water above the infill. When the hydraulic head is high and the  
501 ice filling is thawing, the plug can break, allowing the sand to be transported, and causing a change in the flow regime (as it  
502 was observed in Box 2).

503 Based on the delayed onset of flow into Box 2 and the different flow behavior when compared with Box 1, we suggest that the  
504 two boxes collect two different flow pathways which have some common parts. As Box 1 and Box 2 are located approximately  
505 3 m apart, we suggest that the fracture network is complex under the north face. Some parts of the network contain sand-size  
506 sediments, which probably explain the late and lower flow of Box 2. Other parts of the network lack sand filling and have a  
507 different hydraulic behavior. The effect of the sediment infill on fracture hydrology should be investigated further.

### 508 **5.3. Deciphering possible water sources**

509 According to the fluorescence data and the water flow timing, much of the collected water originates directly from recent  
510 snowmelt. This is also supported by the stable isotopes analysis of water samples from Box 1 (Figure 10) which display values  
511 that are consistent with those reported in high-elevation mountain regions, such as the Alps (Lauber and Goldscheider, 2014),  
512 the Pyrenees (Herms et al., 2019), and Northern China mountains (Sun et al., 2016). It is also very likely that rain in late  
513 summer infiltrated the rock fractures and contributed to the flow. However, some data also hints at other possible sources of  
514 water. First, even the lowest values of electric conductivity of the water are far above the expected snow melt conductivity and  
515 they steadily rise with decreasing flow rate. The surprisingly high electric conductivity found in some samples collected from  
516 fractures ( $>400 \mu\text{S}/\text{cm}$ ) can point to long residence times in the rock. Considering the results from the fluorescent dyes and  
517 the hydrological behavior, the flow path is very short (in both distance and time), thus ruling out a long exchange time between  
518 the surface water and the rock. It is possible that recent meteoric water was mixed with older water that was trapped as ice in  
519 the permafrost-affected rocks. This is also supported by the observed change in the shape of the recession curves over time  
520 (Figure 9). The recession curves at the beginning of the melting season (May-June) show values of  $b \approx 1$  and fit well with the  
521 exponential form that is expressed in Equation 1. The early-season recession curves are also characterized by high values of  
522 'a'. Over time, the value of 'b' increases linearly to a form better described by Equation 3, while the value of the 'a' coefficient  
523 decreases. This change in recession form (Figure S4), from aquifer-type (Equation 1) to channel-type (Equation 3) can be  
524 explained by the thawing of ice in wide sub-vertical fractures that are likely to react more individually (rather than as a network)  
525 and enable rapid flow in the fractured granite. The decrease of 'a' is non-trivial since one could expect that the drainage would  
526 be more efficient and with shorter recession time (i.e. higher 'a' values) as the thawing of ice in the rock fractures progresses.  
527 We thus suggest that the observed decrease in 'a' is due to a gradual change in the water source. As less water drains from the  
528 surface (after the complete thawing of the winter snow) and more water drains from the subsurface ice trapped in the fractures,  
529 the hydraulic gradient is reduced, and the duration of the recession is extended. Another evidence of a possible fossilized  
530 source can be seen in samples collected from Box 2 on 28 July (BOX2\_28JUL, BCKT2\_28JUL) which show an isotopic signal  
531 that is distant from the meteoric water line (Figure 10). One possible explanation is an extended residence time within the  
532 fracture system, allowing for interactions with the surrounding rock. Water samples collected during the peak of summer, on  
533 July 28 (BOX2\_28JUL, BCKT2\_28JUL) and August 9 (BOX1\_9AUG, BCKT2\_9AUG), from both collection systems (Box  
534 1 and Box 2) exhibit relatively enriched  $\delta^{18}\text{O}$  and  $\delta\text{D}$  values compared to those taken in early summer and fall. This enrichment

535 may indicate the partial melting of seasonal snow. In contrast, two other samples from different locations within the AdM  
536 tunnels (TNL\_9AUG and BRCK\_28JUL), collected on the same dates, do not show this enrichment. The observed  $\delta^{18}\text{O}$  and  
537  $\delta\text{D}$  enrichment during summer is consistent with findings from the Alps (Lauber and Goldscheider, 2014; Novel, 1995).  
538 From a permafrost perspective, the thawing of large volumes of fossilized water in permafrost-affected rock could be related  
539 to a thickening of the active layer and degradation of high mountain permafrost - a regional phenomenon seen in recent decades  
540 in boreholes in the Alps and other mountain ranges (Magnin et al., 2024; Noetzli et al., 2024), but never observed directly in  
541 water samples from fractures.  
542 The absence of a signal from sulphorhodamine-B tracer in the water from the upper ledge could be due to excess dilution of  
543 the tracer solution with the snowmelt water, resulting in concentrations below the sensor sensitivity. In 2023, a different dye  
544 was used (fluorescein), with a significantly higher concentration (see Sect. 3.1), and was clearly detected, confirming that the  
545 absence of a sulphorhodamine-B signal in 2022 was due to dilution.

#### 546 **5.4. Implications for alpine geomorphology, hydrogeology, and permafrost**

547 The quantity, timing, and characteristics of water that infiltrates in the fractured, permafrost-affected rocks are important  
548 factors in many geomorphological, hydrological, and geomechanical processes. However, our understanding of the parameters  
549 controlling these factors is limited, as is the ability to measure them. For example, the timing and quantity of water availability  
550 from snowmelt are often estimated indirectly using numerical models of energy and water mass balance (Ben-Asher et al.,  
551 2023; Lehning et al., 1999; Leinauer et al., 2021) and snowpack physics (Lehning et al., 1999; Vionnet et al., 2012). However,  
552 the outputs of such models depend strongly on the meteorological forcing used to drive them, and on hydrogeological  
553 parameters that are usually poorly constrained. The results of this study provide direct observations that can help to reduce  
554 these uncertainties and improve our understanding of water availability for infiltration and its environmental controls.  
555 The new information that we provide regarding water flow in permafrost rock fractures can also be used to improve coupled  
556 heat and water flow models, as it provides the parameters needed to calculate heat advection from the surface (flow rate and  
557 water temperature). The average water temperature measured during flow events is 6.1 °C (Figure 11).  
558 Several recent studies suggest that water-related processes are driving rockwall instability in mountain permafrost (Cathala et  
559 al., 2024; Gruber et al., 2004; Krautblatter et al., 2012; Magnin and Josnin, 2021). Analysis of 1152 rockfall events in the Mont  
560 Blanc massif between 2015-2021 (Magnin et al., 2023; Ravanel and Deline, 2013) shows that 96% of the events occurred  
561 between June and September, with the highest numbers in July, before the maximum depth of the seasonal active layer was  
562 reached (Magnin et al., 2023), possibly due to enhanced water flows when snow melts in the early summer.  
563 The cable car to AdM has been operating since the 1950s. The staff of the operating company of the site reported that significant  
564 water flow from the fractures in the tunnel began in the particularly hot summer of 2015. While the reason for the initiation of  
565 the observed seasonal flow remains unclear, it is reasonable to suggest that it is related to the gradual heating of the rock mass  
566 in AdM and the development of the active layer that is observed in monitored boreholes in the site (Magnin et al., 2024). This

567 suggests that the environmental conditions in AdM are in a transient state and have reached a threshold that triggers substantial  
568 water availability to fractures in the permafrost rocks.

## 569 **5.5. Outlook and Future Directions**

570 Future investigations could build upon this study by conducting more detailed chemical analyses of dissolved elements, which  
571 would help constrain water–rock interaction processes and potential solute sources. Characterizing the mineralogy and size  
572 distribution of sediments flushed from fractures could provide complementary evidence regarding transport pathways and  
573 mechanical erosion. Further stable isotope analyses, combined with absolute dating techniques (e.g., tritium–helium,  
574 radiocarbon, or noble gas methods), could enable a clearer distinction to be made between modern meltwater, rainfall, and  
575 contributions from older subsurface ice. Together, these approaches would refine our understanding of fracture-scale  
576 hydrology in steep permafrost rock walls and how sensitive it is to climate change.

## 577 **6. Conclusions**

578 This study presents novel, direct observations of water infiltration in a high mountain permafrost rock wall, providing rare  
579 field data on processes that are typically poorly understood and rarely monitored. A two-year monitoring system was installed  
580 inside man-made tunnels at the Aiguille du Midi (3842 m a.s.l.) in the Mont Blanc massif to track real-time water flow,  
581 temperature, electrical conductivity, and the infiltration of fluorescent tracers injected into the overlying snowpack. These  
582 measurements were then combined with GST and meteorological data to investigate the origin, timing, and dynamics of water  
583 flow in permafrost-affected fractured rock.

584 Our main findings are:

- 585 • Water flow in fractures is seasonal and begins when AT exceeded 0 °C. Steady flow with daily oscillations began when  
586 GST rose above 0°C, which occurred several weeks (in 2022) or days (in 2023) after the initiation of flow.
- 587 • This flow contained the dye tracer that had been inserted into the snowpack above the tunnel.
- 588 • Fluorescent tracers were detected in the first water flow in early summer and in the flow that followed until mid-summer.  
589 This confirms that the main source of water is snowmelt from the winter snowpack.
- 590 • In snow-free conditions, during late summer, rain also contributes to the flow.
- 591 • The peak flow shows short lag times relative to the peaks of air and ground temperatures (3–9 h and 0–3 h, respectively),  
592 indicating rapid, unsaturated infiltration pathways.
- 593 • Evidence from electrical conductivity measurements, stable water isotopes, and analysis of recession curves suggests that  
594 water stored in the rock is contributing to the flow, possibly from the melting of older ice within the fracture system.  
595 Further investigation is needed to determine the origin of water with high electrical conductivity and a unique isotopic  
596 signature. However, if confirmed, it would provide direct evidence of the melting of fossil ice and permafrost degradation.

- 597 • Distinct flow regimes of flow collected from two nearby fractures in Boxes 1 2 demonstrate a heterogeneous fracture  
598 network with varying sediment infill. It reveals the existence of fractures directly linked to the surface on the one hand,  
599 and fractures with sand infill and likely ice fill with a longer transfer time on the other hand. Moreover, the hydraulic  
600 characteristics of the fractures show unsaturated flow with preferential paths at the end of each warm season before the  
601 active layer freezes again.
- 602 • Water temperatures often exceed 5 °C; together with the intense water flow measured, it strongly suggests that advective  
603 heat transfer likely contributes to ice melting within the rock mass.
- 604 This work provides direct empirical evidence of how surface water infiltrates permafrost rock walls and interacts with the  
605 surface and internal fracture systems. These findings are crucial for the development of coupled hydro-thermal models and  
606 understanding how climate warming affects permafrost degradation, water pathways, and slope stability. This approach and  
607 its results can help future studies that aim to characterize hydrogeological processes in high-elevation rock fractures, identify  
608 early signs of geomorphic instability, and assess the vulnerability of alpine permafrost landscapes in the context of ongoing  
609 climate change.

#### 610 **Author contribution**

611 MB, JYJ, FM: Conceptualization, Data curation, Investigation, Formal analysis, Methodology, Writing.

612 AC: Data curation, Investigation, Formal analysis, Methodology, Writing.

613 JB: Investigation, Writing.

614 EM: Investigation, Methodology.

615 AP: Resources.

616 YP: Data curation, Methodology.

#### 617 **Competing interests**

618 The authors declare that they have no conflict of interest

#### 619 **Acknowledgements**

620 We thank the Compagnie du Mont Blanc and the Aiguille du Midi station staff for their support and access to the site. We also  
621 thank UMR 1114 EMMAH laboratory (Environnement Méditerranéen et Modélisation des Agro-Hydrosystèmes) for the stable  
622 isotope analysis. We are grateful for the assistance of Marine Quiers in planning and applying fluorescence techniques. This  
623 research has been supported by the Agence Nationale de la Recherche (WISPER project, no. ANR-19-CE01-0018).

624        **References**

- 625 Allen, S. K., Gruber, S., and Owens, I. F.: Exploring steep bedrock permafrost and its relationship with recent slope failures  
626 in the Southern Alps of New Zealand, *Permafr. Periglac. Process.*, 20, 345–356, <https://doi.org/10.1002/ppp.658>, 2009.
- 627 Bast, A., Kenner, R., and Phillips, M.: Short-term cooling, drying, and deceleration of an ice-rich rock glacier, *The Cryosphere*,  
628 18, 3141–3158, <https://doi.org/10.5194/tc-18-3141-2024>, 2024.
- 629 Ben-Asher, M., Magnin, F., Westermann, S., Malet, E., Berthet, J., Bock, J., Ravanel, L., and Deline, P.: Estimating surface  
630 water availability in high mountain rock slopes using a numerical energy balance model, [https://doi.org/10.5194/esurf-11-899-](https://doi.org/10.5194/esurf-11-899-2023)  
631 2023, 2023.
- 632 Boussinesq, J.: *Essai sur la théorie des eaux courantes*, Impr. nationale, 1877.
- 633 Brennan, K. P., David, R. O., and Borduas-Dedekind, N.: Spatial and temporal variability in the ice-nucleating ability of alpine  
634 snowmelt and extension to frozen cloud fraction, *Atmospheric Chem. Phys.*, 20, 163–180, [https://doi.org/10.5194/acp-20-163-](https://doi.org/10.5194/acp-20-163-2020)  
635 2020, 2020.
- 636 Brutsaert, W. and Nieber, J. L.: Regionalized drought flow hydrographs from a mature glaciated plateau, *Water Resour. Res.*,  
637 13, 637–643, <https://doi.org/10.1029/WR013i003p00637>, 1977.
- 638 Cathala, M., Bock, J., Magnin, F., Ravanel, L., Ben Asher, M., Astrade, L., Bodin, X., Chambon, G., Deline, P., Faug, T.,  
639 Genuite, K., Jaillet, S., Josnin, J.-Y., Revil, A., and Richard, J.: Predisposing, triggering and runout processes at a permafrost-  
640 affected rock avalanche site in the French Alps (Étache, June 2020), *Earth Surf. Process. Landf.*, 49, 3221–3247,  
641 <https://doi.org/10.1002/esp.5881>, 2024.
- 642 Copernicus Climate Change Service (C3S): European State of the Climate 2022, Copernicus Climate Change Service (C3S),  
643 <https://doi.org/10.24381/GVAF-H066>, 2023.
- 644 Copernicus Climate Change Service (C3S): European State of the Climate 2023, Copernicus Climate Change Service (C3S),  
645 <https://doi.org/10.24381/BS9V-8C66>, 2024.
- 646 Deline, P., Gruber, S., Delaloye, R., Fischer, L., Geertsema, M., Giardino, M., Hasler, A., Kirkbride, M., Krautblatter, M.,  
647 Magnin, F., McColl, S., Ravanel, L., and Schoeneich, P.: Ice Loss and Slope Stability in High-Mountain Regions, in: *Snow*  
648 *and Ice-Related Hazards, Risks, and Disasters*, Elsevier, 521–561, <https://doi.org/10.1016/B978-0-12-394849-6.00015-9>,  
649 2015.
- 650 Draebing, D. and Krautblatter, M.: The Efficacy of Frost Weathering Processes in Alpine Rockwalls, *Geophys. Res. Lett.*, 46,  
651 6516–6524, <https://doi.org/10.1029/2019GL081981>, 2019.
- 652 Draebing, D., Krautblatter, M., and Dikau, R.: Interaction of thermal and mechanical processes in steep permafrost rock walls:  
653 A conceptual approach, *Geomorphology*, 226, 226–235, <https://doi.org/10.1016/j.geomorph.2014.08.009>, 2014.
- 654 Dwivedi, R. D., Singh, P. K., Singh, T. N., and Singh, D. P.: Compressive strength and tensile strength of rocks at sub-zero  
655 temperature, *Indian J. Eng. Mater. Sci.*, 5, 43–48, 1998.
- 656 Eppes, M. C. and Keanini, R.: Mechanical weathering and rock erosion by climate-dependent subcritical cracking, *Rev.*  
657 *Geophys.*, 55, 470–508, <https://doi.org/10.1002/2017RG000557>, 2017.
- 658 Erismann, T. H. and Abele, G.: *Dynamics of rockslides and rockfalls*, Springer Science & Business Media, 2001.

- 659 Fey, C., Wichmann, V., and Zangerl, C.: Influence of permafrost degradation and glacier retreat on recent high mountain  
660 rockfall distribution in the eastern European Alps, *Earth Surf. Process. Landf.*, 50, e70063, <https://doi.org/10.1002/esp.70063>,  
661 2025.
- 662 Fischer, L., Amann, F., Moore, J. R., and Huggel, C.: Assessment of periglacial slope stability for the 1988 Tschierwa rock  
663 avalanche (Piz Morteratsch, Switzerland), *Eng. Geol.*, 116, 32–43, <https://doi.org/10.1016/j.enggeo.2010.07.005>, 2010.
- 664 Ford, D. and Williams, P.: *Karst geomorphology and hydrology*, 1st ed., Unwin Hyman, London, 42 pp., 1989.
- 665 Gabrielli, C. P., McDonnell, J. J., and Jarvis, W. T.: The role of bedrock groundwater in rainfall–runoff response at hillslope  
666 and catchment scales, *J. Hydrol.*, 450–451, 117–133, <https://doi.org/10.1016/j.jhydrol.2012.05.023>, 2012.
- 667 Gardent, M., Rabatel, A., Dedieu, J.-P., and Deline, P.: Multitemporal glacier inventory of the French Alps from the late 1960s  
668 to the late 2000s, *Glob. Planet. Change*, 120, 24–37, <https://doi.org/10.1016/j.gloplacha.2014.05.004>, 2014.
- 669 Gruber, S. and Haeberli, W.: Permafrost in steep bedrock slopes and its temperatures-related destabilization following climate  
670 change, *J. Geophys. Res. Earth Surf.*, 112, 1–10, <https://doi.org/10.1029/2006JF000547>, 2007.
- 671 Gruber, S., Hoelzle, M., and Haeberli, W.: Rock-wall temperatures in the Alps: Modelling their topographic distribution and  
672 regional differences, *Permafr. Periglac. Process.*, 15, 299–307, <https://doi.org/10.1002/ppp.501>, 2004.
- 673 Guillet, G., Ravel, L., Beutel, J., and Deline, P.: Fracture kinematics in steep bedrock permafrost, Aiguille du Midi (3842 m  
674 a.s.l., Chamonix Mont-Blanc, France), <https://doi.org/10.3929/ETHZ-B-000309262>, 2018.
- 675 Hales, T. C. and Roering, J. J.: Climatic controls on frost cracking and implications for the evolution of bedrock landscapes,  
676 *J. Geophys. Res.*, 112, F02033–F02033, <https://doi.org/10.1029/2006JF000616>, 2007.
- 677 Hallet, B., Walder, J. S., and Stubbs, C. W.: Weathering by segregation ice growth in microcracks at sustained subzero  
678 temperatures: Verification from an experimental study using acoustic emissions, *Permafr. Periglac. Process.*, 2, 283–300,  
679 <https://doi.org/10.1002/ppp.3430020404>, 1991.
- 680 Hanson, S. and Hoelzle, M.: The thermal regime of the active layer at the Murtèl rock glacier based on data from 2002, *Permafr.*  
681 *Periglac. Process.*, 15, 273–282, <https://doi.org/10.1002/ppp.499>, 2004.
- 682 Hasler, A., Gruber, S., Font, M., and Dubois, A.: Advective heat transport in frozen rock clefts: Conceptual model, laboratory  
683 experiments and numerical simulation, *Permafr. Periglac. Process.*, 22, 378–389, <https://doi.org/10.1002/ppp.737>, 2011.
- 684 Hasler, A., Gruber, S., and Beutel, J.: Kinematics of steep bedrock permafrost, *J. Geophys. Res. Earth Surf.*, 117,  
685 2011JF001981, <https://doi.org/10.1029/2011JF001981>, 2012.
- 686 Herms, I., Jódar, J., Soler, A., Vadillo, I., Lambán, L. J., Martos-Rosillo, S., Núñez, J. A., Arnó, G., and Jorge, J.: Contribution  
687 of isotopic research techniques to characterize high-mountain-Mediterranean karst aquifers: The Port del Comte (Eastern  
688 Pyrenees) aquifer, *Sci. Total Environ.*, 656, 209–230, <https://doi.org/10.1016/j.scitotenv.2018.11.188>, 2019.
- 689 Huggel, C., Allen, S., Deline, P., Fischer, L., Noetzli, J., and Ravel, L.: Ice thawing, mountains falling—are alpine rock slope  
690 failures increasing, *Geol. Today*, 28, 98–104, <https://doi.org/10.1111/j.1365-2451.2012.00836.x>, 2012.
- 691 Krakauer, N. Y. and Temimi, M.: Stream recession curves and storage variability in small watersheds, *Hydrol. Earth Syst.*  
692 *Sci.*, 15, 2377–2389, <https://doi.org/10.5194/hess-15-2377-2011>, 2011.

- 693 Krautblatter, M., Huggel, C., Deline, P., and Hasler, A.: Research Perspectives on Unstable High-alpine Bedrock Permafrost:  
694 Measurement, Modelling and Process Understanding, *Permafr. Periglac. Process.*, 23, 80–88, <https://doi.org/10.1002/ppp.740>,  
695 2012.
- 696 Krautblatter, M., Funk, D., and Günzel, F. K.: Why permafrost rocks become unstable: A rock-ice-mechanical model in time  
697 and space, *Earth Surf. Process. Landf.*, 38, 876–887, <https://doi.org/10.1002/esp.3374>, 2013.
- 698 Lauber, U. and Goldscheider, N.: Use of artificial and natural tracers to assess groundwater transit-time distribution and flow  
699 systems in a high-alpine karst system (Wetterstein Mountains, Germany), *Hydrogeol. J.*, 22, 1807–1824,  
700 <https://doi.org/10.1007/s10040-014-1173-6>, 2014.
- 701 Legay, A., Magnin, F., and Ravanel, L.: Rock temperature prior to failure: Analysis of 209 rockfall events in the Mont Blanc  
702 massif (Western European Alps), *Permafr. Periglac. Process.*, 32, 520–536, <https://doi.org/10.1002/ppp.2110>, 2021.
- 703 Lehning, M., Bartelt, P., Brown, B., Russi, T., Stöckli, U., and Zimmerli, M.: snowpack model calculations for avalanche  
704 warning based upon a new network of weather and snow stations, *Cold Reg. Sci. Technol.*, 30, 145–157,  
705 [https://doi.org/10.1016/S0165-232X\(99\)00022-1](https://doi.org/10.1016/S0165-232X(99)00022-1), 1999.
- 706 Leinauer, J., Jacobs, B., and Krautblatter, M.: High alpine geotechnical real time monitoring and early warning at a large  
707 imminent rock slope failure (Hochvogel, GER/AUT), *IOP Conf. Ser. Earth Environ. Sci.*, 833, <https://doi.org/10.1088/1755-1315/833/1/012146>, 2021.
- 709 Li, N., Zhang, P., Chen, Y., and Swoboda, G.: Fatigue properties of cracked, saturated and frozen sandstone samples under  
710 cyclic loading, *Int. J. Rock Mech. Min. Sci.*, 40, 145–150, [https://doi.org/10.1016/S1365-1609\(02\)00111-9](https://doi.org/10.1016/S1365-1609(02)00111-9), 2003.
- 711 Magnin, F. and Josnin, J.-Y.: Water Flows in Rockwall Permafrost : a Numerical Approach Coupling Hydrological and  
712 Thermal Processes, *J. Geophys. Res. Earth Surf.*, 2021.
- 713 Magnin, F., Brenning, A., Bodin, X., Deline, P., and Ravanel, L.: Modélisation statistique de la distribution du permafrost de  
714 paroi : application au massif du Mont Blanc, *Géomorphologie Relief Process. Environ.*, 21, 145–162,  
715 <https://doi.org/10.4000/geomorphologie.10965>, 2015a.
- 716 Magnin, F., Deline, P., Ravanel, L., Noetzli, J., and Pogliotti, P.: Thermal characteristics of permafrost in the steep alpine rock  
717 walls of the Aiguille du Midi (Mont Blanc Massif, 3842 m a.s.l), *Cryosphere*, 9, 109–121, <https://doi.org/10.5194/tc-9-109-2015>, 2015b.
- 719 Magnin, F., Ravanel, L., Ben-Asher, M., Bock, J., Cathala, M., Duvillard, P.-A., Jean, P., Josnin, J.-Y., Kaushik, S., Revil, A.,  
720 and Deline, P.: From Rockfall Observation to Operational Solutions: Nearly 20 years of Cryo-gravitational Hazard Studies in  
721 Mont-Blanc Massif, *Rev. Géographie Alp.*, 111–2, <https://doi.org/10.4000/rga.11703>, 2023.
- 722 Magnin, F., Ravanel, L., Bodin, X., Deline, P., Malet, E., Krysiecki, J., and Schoeneich, P.: Main results of permafrost  
723 monitoring in the French Alps through the *PermaFrance* network over the period 2010–2022, *Permafr. Periglac. Process.*, 35,  
724 3–23, <https://doi.org/10.1002/ppp.2209>, 2024.
- 725 Maillet, E. T.: *Essais d'hydraulique souterraine & fluviale*, A. Hermann, 1905.
- 726 Manning, A. H. and Caine, J. S.: Groundwater noble gas, age, and temperature signatures in an Alpine watershed: Valuable  
727 tools in conceptual model development, *Water Resour. Res.*, 43, 2006WR005349, <https://doi.org/10.1029/2006WR005349>,  
728 2007.

- 729 Marcer, M., Ringsø Nielsen, S., Ribeyre, C., Kummert, M., Duvillard, P., Schoeneich, P., Bodin, X., and Genuite, K.:  
 730 Investigating the slope failures at the Lou rock glacier front, French Alps, *Permafr. Periglac. Process.*, 31, 15–30,  
 731 <https://doi.org/10.1002/ppp.2035>, 2020.
- 732 Maréchal, J. C., Perrochet, P., and Tacher, L.: Long-term simulations of thermal and hydraulic characteristics in a mountain  
 733 massif: The Mont Blanc case study, French and Italian Alps, *Hydrogeol. J.*, 7, 341–354,  
 734 <https://doi.org/10.1007/s100400050207>, 1999.
- 735 Maréchal, J.-C.: Les circulations d’eau dans les massifs cristallins alpins et leurs relations avec les ouvrages souterrains, EPFL,  
 736 <https://doi.org/10.5075/epfl-thesis-1769>, 1998.
- 737 Matsuoka, N. and Murton, J.: Frost weathering: recent advances and future directions, *Permafr. Periglac. Process.*, 19, 195–  
 738 210, <https://doi.org/10.1002/ppp.620>, 2008.
- 739 Matsuoka, N. and Sakai, H.: Rockfall activity from an alpine cliff during thawing periods, *Geomorphology*, 28, 309–328,  
 740 [https://doi.org/10.1016/S0169-555X\(98\)00116-0](https://doi.org/10.1016/S0169-555X(98)00116-0), 1999.
- 741 Mellor, M.: Mechanical properties of rocks at low temperatures, in: 2nd International Conference on Permafrost, Yakutsk,  
 742 International Permafrost Association, 334–344, 1973.
- 743 Noetzli, J., Isaksen, K., Barnett, J., Christiansen, H. H., Delaloye, R., Etzelmüller, B., Farinotti, D., Galleman, T., Guglielmin,  
 744 M., Hauck, C., Hilbich, C., Hoelzle, M., Lambiel, C., Magnin, F., Oliva, M., Paro, L., Pogliotti, P., Riedl, C., Schoeneich, P.,  
 745 Valt, M., Vieli, A., and Phillips, M.: Enhanced warming of European mountain permafrost in the early 21st century, *Nat.*  
 746 *Commun.*, 15, 10508, <https://doi.org/10.1038/s41467-024-54831-9>, 2024.
- 747 Pellet, C. and Hauck, C.: Monitoring soil moisture from middle to high elevation in Switzerland: set-up and first results from  
 748 the SOMOMOUNT network, *Hydrol. Earth Syst. Sci.*, 21, 3199–3220, <https://doi.org/10.5194/hess-21-3199-2017>, 2017.
- 749 Phillips, M., Haberkorn, A., Draebing, D., Krautblatter, M., Rhyner, H., and Kenner, R.: Seasonally intermittent water flow  
 750 through deep fractures in an Alpine Rock Ridge: Gemsstock, Central Swiss Alps, *Cold Reg. Sci. Technol.*, 125, 117–127,  
 751 <https://doi.org/10.1016/j.coldregions.2016.02.010>, 2016.
- 752 Ravanel, L. and Deline, P.: Climate influence on rockfalls in high-alpine steep rockwalls: The north side of the aiguilles de  
 753 chamonix (mont blanc massif) since the end of the “Little Ice Age,” *Holocene*, 21, 357–365,  
 754 <https://doi.org/10.1177/0959683610374887>, 2011.
- 755 Ravanel, L. and Deline, P.: A network of observers in the Mont-Blanc massif to study rockfall from high Alpine rockwalls,  
 756 *Geogr. Fis. E Din. Quat.*, 151–158, <https://doi.org/10.4461/GFDQ.2013.36.12>, 2013.
- 757 Ravanel, L., Magnin, F., and Deline, P.: Impacts of the 2003 and 2015 summer heatwaves on permafrost-affected rock-walls  
 758 in the Mont Blanc massif, *Sci. Total Environ.*, 609, 132–143, <https://doi.org/10.1016/j.scitotenv.2017.07.055>, 2017.
- 759 Scandroglio, R., Stoll, V., and Krautblatter, M.: The driving force of all nature. Modelling water pressure and its stability  
 760 consequences on alpine bedrock slopes, *IOP Conf. Ser. Earth Environ. Sci.*, 833, <https://doi.org/10.1088/1755-1315/833/1/012109>, 2021.
- 762 Scandroglio, R., Weber, S., Rehm, T., and Krautblatter, M.: Decadal in situ hydrological observations and empirical modeling  
 763 of pressure head in a high-alpine, fractured calcareous rock slope, *Earth Surf. Dyn.*, 13, 295–314, <https://doi.org/10.5194/esurf-13-295-2025>, 2025.

- 765 Scherler, M., Hauck, C., Hoelzle, M., Stähli, M., and Völksch, I.: Meltwater infiltration into the frozen active layer at an alpine  
766 permafrost site, *Permafr. Periglac. Process.*, 21, 325–334, <https://doi.org/10.1002/ppp.694>, 2010.
- 767 Smith, R. E. (Ed.): *Infiltration theory for hydrologic applications*, American Geophysical Union, Washington, DC, 1 pp.,  
768 <https://doi.org/10.1029/WM015>, 2002.
- 769 Staub, B. and Delaloye, R.: Using Near-Surface Ground Temperature Data to Derive Snow Insulation and Melt Indices for  
770 Mountain Permafrost Applications: Snow and Melt Indices Derived from GST Data, *Permafr. Periglac. Process.*, 28, 237–248,  
771 <https://doi.org/10.1002/ppp.1890>, 2017.
- 772 Strauhal, T., Loew, S., Holzmann, M., and Zangerl, C.: Detailed hydrogeological analysis of a deep-seated rockslide at the  
773 Gepatsch reservoir (Klasgarten, Austria), *Hydrogeol. J.*, 24, 349–371, <https://doi.org/10.1007/s10040-015-1341-3>, 2016.
- 774 Su, G. W., Geller, J. T., Pruess, K., and Hunt, J.: Overview of preferential flow in unsaturated fractures, *Geophys. Monogr. Ser.*,  
775 122, 147–155, <https://doi.org/10.1029/GM122p0147>, 2000.
- 776 Sun, Z., Ma, R., Wang, Y., Ma, T., and Liu, Y.: Using isotopic, hydrogeochemical-tracer and temperature data to characterize  
777 recharge and flow paths in a complex karst groundwater flow system in northern China, *Hydrogeol. J.*, 24, 1393–1412,  
778 <https://doi.org/10.1007/s10040-016-1390-2>, 2016.
- 779 Tallaksen, L. M.: A review of baseflow recession analysis, *J. Hydrol.*, 165, 349–370, [https://doi.org/10.1016/0022-1694\(94\)02540-R](https://doi.org/10.1016/0022-1694(94)02540-R), 1995.
- 781 Thompson, S. S., Kulessa, B., Essery, R. L. H., and Lüthi, M. P.: Bulk meltwater flow and liquid water content of snowpacks  
782 mapped using the electrical self-potential (SP) method, *The Cryosphere*, 10, 433–444, <https://doi.org/10.5194/tc-10-433-2016>,  
783 2016.
- 784 Tsang, C.-F., Tsang, Y. W., Birkhölzer, J., and Moreno, L.: Dynamic Channeling of Flow and Transport in Saturated and  
785 Unsaturated Heterogeneous Media, in: *Geophysical Monograph Series*, edited by: Evans, D. D., Nicholson, T. J., and  
786 Rasmussen, T. C., American Geophysical Union, Washington, D. C., 33–44, <https://doi.org/10.1029/GM042p0033>, 2013.
- 787 Vionnet, V., Brun, E., Morin, S., Boone, A., Faroux, S., Le Moigne, P., Martin, E., and Willemet, J.-M.: The detailed snowpack  
788 scheme Crocus and its implementation in SURFEX v7.2, *Geosci. Model Dev.*, 5, 773–791, <https://doi.org/10.5194/gmd-5-773-2012>, 2012.
- 790 Walter, F., Amann, F., Kos, A., Kenner, R., Phillips, M., de Preux, A., Huss, M., Tognacca, C., Clinton, J., Diehl, T., and  
791 Bonanomi, Y.: Direct observations of a three million cubic meter rock-slope collapse with almost immediate initiation of  
792 ensuing debris flows, *Geomorphology*, 351, 106933–106933, <https://doi.org/10.1016/j.geomorph.2019.106933>, 2020.
- 793 Weber, S., Beutel, J., Faillettaz, J., Hasler, A., Krautblatter, M., and Vieli, A.: Quantifying irreversible movement in steep,  
794 fractured bedrock permafrost on Matterhorn (CH), *Cryosphere*, 11, 567–583, <https://doi.org/10.5194/tc-11-567-2017>, 2017.
- 795